International Journal of Solids and Structures 302 (2024) 112987

Contents lists available at ScienceDirect

International Journal of Solids and Structures

journal homepage: www.elsevier.com/locate/ijsolstr

A numerical study on tensile strength of low-density Kagome networks made of brittle fibers

Soham M. Mane, Kenneth M. Liechti, Rui Huang *

Department of Aerospace Engineering and Engineering Mechanics, University of Texas, Austin, TX 78712, USA

ARTICLE INFO

Keywords:
Kagome network
Tensile strength
Buckling
Damage
Toughness

ABSTRACT

In this paper, we present a numerical study on the tensile strength of low-density Kagome networks made of brittle fibers. First, an elastic beam model is employed to analytically predict the effective elastic properties and tensile strength, as well as the critical condition for buckling of the fibers in Kagome networks. A series of finite element analyses are then conducted to simulate the elastic deformation and failure of Kagome networks under tension. The numerical results based on unit-cell models reveal four possible failure modes of the Kagome networks subject to uniaxial tension, summarized in a phase diagram in terms of the relative density and the fiber strength. The pre-buckling failure mode is restricted to cases with relatively high density and low fiber strength. A low-density Kagome network is likely to fail by one of the post-buckling modes, with an effective tensile strength much lower than the prediction by the elastic beam model. For Kagome networks consisting of a large number of unit cells, the effect of boundary conditions on the tensile strength is examined. Under periodic boundary conditions, the effective tensile strength is nearly identical to that predicted by the unit-cell model, independent of the model size. Under a roller boundary condition, with damage initiation near the free edges followed by a diffusive damage progression, the effective tensile strength is lower than that under periodic boundary conditions for the cases of relatively low fiber strengths. Under a clamped boundary condition, the effective tensile strength is higher than that under periodic boundary conditions for the cases of relatively high fiber strengths, where fiber buckling is largely suppressed by the clamped boundaries. Finally, the effect of a crack-like defect on the effective tensile strength is studied for Kagome networks under the clamped boundary condition. With a small defect, the effective strength is nearly independent of the defect size. In contrast, with a relatively long defect, the effective strength decreases almost linearly with the length of the crack-like defect. The effective toughness for damage initiation and steady-state damage progression in the Kagome networks is discussed from an energetic perspective.

1. Introduction

Micro-architectured materials offer the opportunity of obtaining unique combinations of material properties, such as high strength and fracture toughness at low density (Fleck et al., 2010; Schwaiger et al., 2019; Liu et al., 2020). In particular, two-dimensional (2D) and three-dimensional (3D) periodic lattice or network structures have been hierarchically architected to achieve lightweight, flaw-tolerant, and ultra-strong mechanical properties (Meza et al., 2014; Meza et al, 2015; Xia et al., 2019; Zhang et al., 2019). This work focuses on 2D network structures. Fig. 1 shows three periodic 2D networks and their unit cells, including Kagome, triangular, and square networks. Each network is made from uniform, long fibers. For such a periodic 2D network, the relative density can be written approximately as

$$\rho = \frac{Ad}{L}, \tag{1.1}$$

where A is a constant depending on the network topology and the cross section of the fibers, L is the length of a fiber segment between two adjacent joints, and d is the thickness of the fiber. Table 1 lists the values of A for the three periodic 2D networks made from fibers with a square cross section, as presented in Romijn and Fleck (2007). The values of A are slightly different for networks of fibers with a circular cross section (Mane et al., 2021). It should be noted that Eq. (1.1) is a good approximation only for low-density 2D networks (e.g., $\rho < 0.2$).

A periodic 2D network behaves like a linearly elastic material if the

* Corresponding author.
E-mail address: ruihuang@mail.utexas.edu (R. Huang).

https://doi.org/10.1016/j.ijsolstr.2024.112987
Received 16 February 2024; Received in revised form 9 July 2024; Accepted 12 July 2024
Available online 15 July 2024

overall deformation is small. The linearly elastic properties of periodic networks have been predicted analytically (Gibson and Ashby, 1997; Christensen, 2000; Ostoja-Starzewski, 2002; Wang and McDowell, 2004). Assuming linear elasticity for the fiber material and rigid (welded) joints between the fibers, the effective Young's modulus (E_{eff}) of a periodic 2D network depends on the relative density and can be written as:

$$E_{eff} = B\rho^b E_f, \tag{1.2}$$

where E_f is Young's modulus of the fiber material, B and b are constants depending on the network topology (see Table 1; Romijn and Fleck, 2007). Both the Kagome and triangular networks are isotropic with a linear scaling for the effective Young's modulus ($b = 1$). In contrast, the square network is highly anisotropic with a different scaling ($b = 3$) for the effective Young's modulus in the $\pm$ 45° rotated direction. The linear scaling ($b = 1$) of the effective Young's modulus indicates stretch-dominated fiber deformation when the network is subject to uniaxial tension, whereas the cubic scaling ($b = 3$) indicates bending-dominated deformation of the fibers. It should be noted that the analytical prediction for the effective Young's modulus is applicable only in the linearly elastic regime. In the case of a low-density Kagome or triangular network, buckling of fibers may lead to highly nonlinear elastic deformation even at small strains (Mane et al., 2021).

Beyond elasticity, inelastic mechanical properties such as strength and toughness of periodic 2D networks have also been studied extensively (Gibson and Ashby, 1997; Wang and McDowell, 2004; Fleck and Qiu, 2007; Romijn and Fleck, 2007; Lipperman et al., 2007; Quintana Alonso et al., 2010; Cui et al., 2011; Tankasala et al., 2015; Gu et al., 2018; Luan et al., 2022; Shaikeea et al., 2022). In particular, the effective tensile strength of a periodic 2D network may be estimated using a linearly elastic truss model, where all the joints are assumed to be pin joints so that each fiber segment is subject to axial tension or compression. Assuming that the fiber material is linearly elastic and brittle, with a tensile strength S_f, failure of the network initiates when the tensile stress in at least one of the fiber segments reaches its tensile strength. The effective tensile strength of the network, S_{eff}, is then determined by the corresponding force and the effective cross-section area of the network. For the periodic Kagome, triangular and square networks made of fibers with a square cross section, the effective tensile strength in the x and y directions (0/90°) can be written as

$$S_{eff} = C\rho^c S_f, \tag{1.3}$$

where the constants C and c depend on the network topology, as listed in Table 1 (Fleck and Qiu, 2007).

The truss model assumes that the fibers undergo stretch-dominated deformation and thus predicts $c = 1$ for the effective tensile strength. However, for the square network, this assumption is valid only when it is subject to uniaxial tension in the x or y direction (0/90°). When a square network is subject to uniaxial tension in the $\pm$ 45° direction, the truss model (with pin joints) would predict a zero Young's modulus until all fibers are aligned in the loading direction. As noted in previous works (Wang and McDowell, 2004; Romijn and Fleck, 2007; Mane et al., 2021), the elastic deformation of a square network loaded in the $\pm$ 45° direction is primarily due to bending of the fibers (assuming rigid joints). In this case, an elastic beam model can be used to estimate its effective Young's modulus and strength, which predicts a cubic scaling ($b = 3$) for the Young's modulus and a quadratic scaling ($c = 2$) for the effective tensile strength (Mane, 2023).

For the Kagome and triangular networks, the truss model can be justified if the effect of fiber bending is negligible compared to fiber stretching. Previously, Fleck and Qiu (2007) considered the effective strengths of the Kagome and triangular networks, with $C = 1/2$ in Eq. (1.3) for the Kagome network subject to uniaxial tension in the y direction (90°), and $C = 1/3$ for the triangular network subject to uniaxial tension in the x direction (0°). It has been found that, based on the truss model, the effective strength is anisotropic for both the Kagome and triangular networks, with $C = 1/3$ in the x direction (0°) and $C = 1/2$ in the y direction (90°), in spite of the six-fold symmetry of the network topology and the isotropic, linearly elastic behavior of both networks. Similar anisotropy has been observed both numerically and experimentally in the effective yield strength of triangular networks made of an aluminum alloy (Gu et al., 2018). The effective tensile strength is lower in the x direction (0°) because only 1/3 of the fibers that are parallel to the loading direction are stressed, and the other 2/3 of the fibers are not stressed at all under uniaxial tension (according to the truss model). In contrast, when subject to uniaxial tension in the y-direction (90°), all fibers are stressed, 2/3 of the fibers in tension and 1/3 in compression (perpendicular to the loading direction), giving rise to a higher effective tensile strength. In this case, the truss model is valid only if the fibers in compression do not buckle. However, for a low-density Kagome or triangular network, fiber buckling may occur at a small strain (Mane et al., 2021), and consequently, the effective tensile strength could be considerably lower than predicted by the truss model. To our knowledge, the effect of buckling on the effective tensile strength has not been systematically studied in the literature. An additional consequence of buckling is that the potential failure mode may change

Table 1
Scaling parameters for the effective properties of periodic 2D networks.

	Kagome (0°)	Kagome (90°)	Triangular (0°)	Triangular (90°)	Square (0/90°)	Square (±45°)
A	$\sqrt{3}$	$\sqrt{3}$	$2\sqrt{3}$	$2\sqrt{3}$	2	2
B	$\frac{1}{3}$	$\frac{1}{3}$	$\frac{1}{3}$	$\frac{1}{3}$	$\frac{1}{2}$	$\frac{1}{4}$
b	1	1	1	1	1	3
C	$\frac{1}{3}$	$\frac{1}{2}$	$\frac{1}{3}$	$\frac{1}{2}$	$\frac{1}{2}$	$\frac{1}{6}$
c	1	1	1	1	1	2

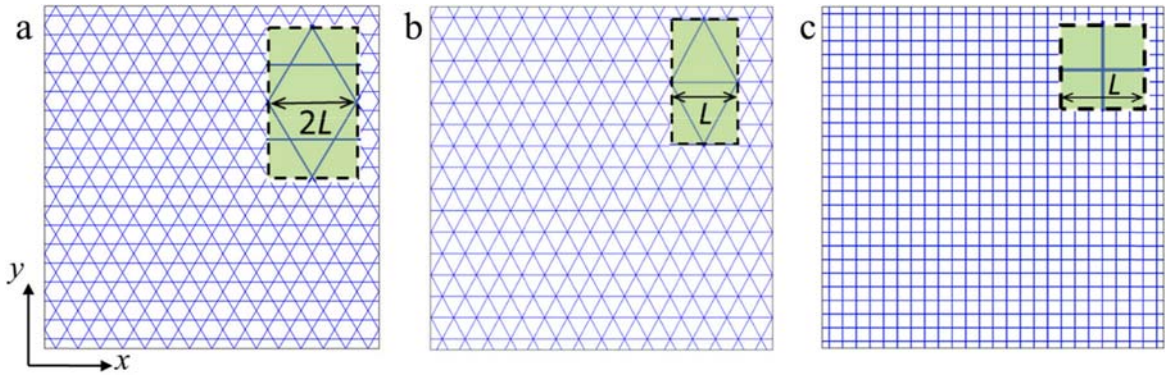

Fig. 1. Periodic 2D networks made of long fibers: (a) Kagome, (b) triangular, and (c) square. Insets show unit cells with segment length L.

from stretch-dominated to bending-dominated, leading to different scaling for the effective strength.

In the remainder of this paper, we focus on low-density Kagome networks, where the effects of fiber buckling are significant for the effective tensile strength and the associated failure modes. Section 2 presents an elastic beam model to analytically predict the effective elastic properties and tensile strength, as well as the critical condition for fiber buckling in Kagome networks. A finite element method is presented in Section 3 for simulating the elastic deformation and failure of Kagome networks under tension. Section 4 discusses the numerical results based on unit-cell models of Kagome networks. The effects of model size and boundary conditions are examined in Section 5, followed by a study on the effect of crack-like defects in Section 6. We conclude in Section 7 with a summary.

2. Analytical predictions

Elastic beam models have been used to predict the effective tensile strength of hexagonal networks (Gibson and Ashby, 1997). In an elastic beam model, bending of the fibers is taken into account along with stretching. The local stress in the fiber results from the axial force and bending moment combined. Failure initiates when the maximum local tensile stress reaches the tensile strength of the fiber material, assumed to be linearly elastic and brittle, and the corresponding effective stress of the network defines its effective tensile strength. Here we present an elastic beam model for the Kagome network. Similar models have been developed for the triangular and rotated square networks (Mane, 2023).

For a Kagome network subject to uniaxial tension in the y-direction (Fig. 2), each slanted fiber segment is subject to two end forces (F and N) and two bending moments (M_1 and M_2). The two bending moments are not necessarily equal, because there are two types of joints in the Kagome network. The joint between a slanted fiber and a horizontal fiber can rotate like a rigid body and is called the SH joint. In contrast, the joint between two slanted fibers, called the SS joint, cannot rotate due to symmetry, assuming periodic boundary conditions for the unit cell. In addition, each horizontal fiber segment is subject to a compressive axial force (N) and a bending moment (M_2). Together, each unit cell is subject to a uniaxial force of $2F$ in the y-direction, with zero net force in the x-direction. Thus, the effective nominal stress of the Kagome network is: $\sigma_y = F/(Ld)$, with an effective cross-sectional area of $2Ld$ for the unit cell. Next we determine the force N and the bending moments (M_1 and M_2) by the equilibrium condition and deformation compatibility of the fiber segments.

Referring to the free body diagram in Fig. 2(b), the moment balance requires that

$$M_1 + M_2 = \frac{L}{2}\left(F - \sqrt{3}N\right). \tag{2.1}$$

Since each slanted segment is between an SS joint and an SH joint, and the SS joint cannot rotate, the slanted segment can be treated as a cantilever beam with a fully clamped end at the SS joint, subject to two forces (F and N) and a bending moment (M_2) at the other end (SH joint). The angle of rotation of the SH joint is then

$$\theta = \frac{L^2}{4E_f I}\left(F - \sqrt{3}N\right) - \frac{M_2 L}{E_f I}, \tag{2.2}$$

where $I = d^4/12$ for the fiber segment with a square cross section.

Meanwhile, each horizontal segment is between two SH joints (Fig. 2c) and can be treated as a simply supported beam subject to a bending moment at each end. Thus, the angle of rotation at each end is

$$\theta = \frac{M_2 L}{2E_f I}. \tag{2.3}$$

Compatibility of deformation requires the angles of rotation to be equal at the rigid joints. With Eq. (2.2) and (2.3), we obtain the bending moment at the SH joints:

$$M_2 = \frac{L}{6}\left(F - \sqrt{3}N\right). \tag{2.4}$$

Then, with Eq. (2.1) and (2.4), we obtain the bending moment at the SS joints:

$$M_1 = \frac{L}{3}\left(F - \sqrt{3}N\right), \tag{2.5}$$

which is twice of the bending moment at the SH joints.

Further, the axial displacement at each end of the horizontal segment is due to the axial force:

$$\delta_x = \frac{NL}{2E_f d^2}, \tag{2.6}$$

whereas the end displacement in the x-direction for the slanted segment is due to both the axial force and bending moment:

$$\delta_x = -\frac{L}{4E_f d^2}\left(\sqrt{3}F + N\right) + \frac{\sqrt{3}L^3}{12E_f I}\left(F - \sqrt{3}N\right) - \frac{\sqrt{3}L^2}{4E_f I}M_2. \tag{2.7}$$

The deformation compatibility requires the end displacements to be equal at the rigid joints. Inserting Eq. (2.4) and Eq. (2.6) into Eq. (2.7), we obtain

$$N = \frac{F}{\sqrt{3}}\left(1 - \frac{d^2}{2L^2}\right)\left(1 + \frac{d^2}{2L^2}\right)^{-1} \approx \frac{F}{\sqrt{3}}\left(1 - \frac{d^2}{L^2}\right), \tag{2.8}$$

where the approximation is taken for a low-density network with $\frac{d^2}{L^2} \ll 1$, retaining two leading order terms. The moments, M_1 and M_2, are then obtained by inserting Eq. (2.8) into Eqs. (2.4) and (2.5).

Moreover, the end displacement in the y-direction for the slanted

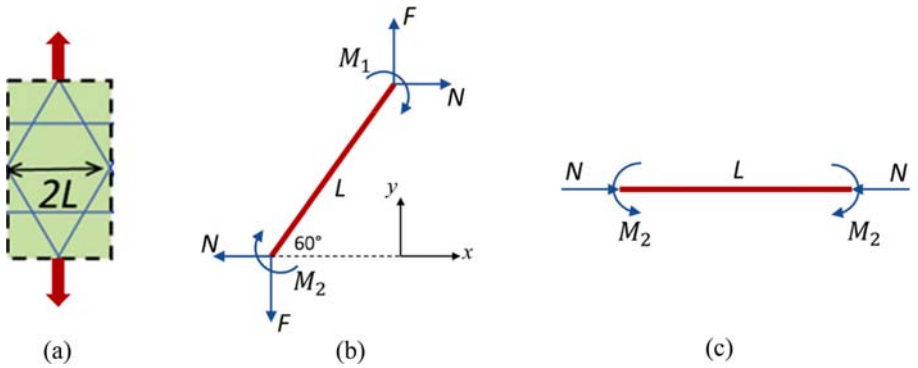

Fig. 2. Elastic beam model for a Kagome network subject to a uniaxial force in the y-direction. (a) A unit cell of the Kagome network; (b) Free body diagram of a slanted fiber segment; (c) Free body diagram of a horizontal fiber segment.

segment is obtained as:

$$\delta_y = \frac{L}{4E_f d^2}\left(3F + \sqrt{3}N\right) + \frac{L^3}{24E_f I}\left(F - \sqrt{3}N\right) \approx \frac{3FL}{2E_f d^2}\left(1 - \frac{5d^2}{6L^2}\right). \tag{2.9}$$

The effective strain components of the unit cell are: $\varepsilon_y = \frac{2\delta_y}{\sqrt{3}L}$ and $\varepsilon_x = -\frac{2\delta_x}{L}$. Thus, with Eqs. (2.6) and (2.9), the effective Poisson's ratio of the Kagome network is:

$$\nu_{eff} \equiv -\frac{\varepsilon_x}{\varepsilon_y} = \sqrt{3}\,\frac{\delta_x}{\delta_y} \approx \frac{1}{3}\left(1 - \frac{d^2}{6L^2}\right). \tag{2.10}$$

Similarly, the effective Young's modulus of the Kagome network is obtained as

$$E_{eff} \equiv \frac{\sigma_y}{\varepsilon_y} \approx \frac{1}{3}\rho E_f\left(1 + \frac{5d^2}{6L^2}\right), \tag{2.11}$$

where $\sigma_y = F/(Ld)$ is the effective nominal stress. For a low-density Kagome network ($\rho = \sqrt{3}d/L \ll 1$), the effective Poisson's ratio and Young's modulus recovers the values predicted by the truss model with $d/L \to 0$, namely, $\nu_{eff} = 1/3$ and $E_{eff} = \frac{1}{3}\rho E_f$. Both Eqs. (2.10) and (2.11) contain additional terms that are quadratic in d/L as the leading-order correction due to the effect of bending stiffness in the elastic beam model. It is noted that the coefficients of these correction terms are different from those listed in Lipperman et al. (2007). However, Lipperman et al. (2007) did not provide the details as to how their results were derived. Thus, it is unclear what could have led to the differences.

With the combined bending moment and axial force, the maximum tensile stress in the fibers occurs in the slanted fiber segment, which is obtained as:

$$\sigma_{max} = \frac{M_1 d}{2I} + \frac{\sqrt{3}F + N}{2d^2} = \frac{2FL}{d^3}\left(1 - \frac{1 - \frac{d^2}{2L^2}}{1 + \frac{d^2}{2L^2}}\right) + \frac{\sqrt{3}F}{2d^2}\left(1 + \frac{1}{3}\frac{1 - \frac{d^2}{2L^2}}{1 + \frac{d^2}{2L^2}}\right). \tag{2.12}$$

With $\sigma_y = F/(Ld)$, the maximum local stress in the fibers is related to the effective stress as

$$\sigma_{max} \approx \sigma_y \frac{2L}{\sqrt{3}d}\left(1 + \frac{\sqrt{3}\,d}{L}\right). \tag{2.13}$$

By setting $\sigma_{max} = S_f$, with S_f being the tensile strength of the fiber material, we obtain the effective tensile strength of the Kagome network as

$$S_{eff} \approx \frac{1}{2}(1 - \rho)\rho S_f. \tag{2.14}$$

Thus, the elastic beam model recovers the truss model for the Kagome network when the relative density is low ($\rho \ll 1$), predicting $c = 1$ and $C = 1/2$ for the effective tensile strength in Eq. (1.3), same as that given in Fleck and Qiu (2007). Notably, the elastic beam model predicts that the maximum tensile stress occurs in the slanted segment near the SS joint where the bending moment is the maximum ($M_1 > M_2$). Thus, damage initiation is expected to occur near the SS joints in the Kagome network subject to uniaxial tension in the y-direction. In contrast, by the truss model, the local stress is uniform in the slanted fibers, and no specific location is predicted for damage initiation. Moreover, the first-order correction to the predicted effective strength in Eq. (2.14) is linear in the relative density ($\rho = \sqrt{3}d/L$), whereas the leading order corrections to the effective elastic properties in Eqs. (2.10–2.11) are quadratic. Therefore, the prediction by the truss model is less accurate for the effective strength than for the effective elastic properties of low-density Kagome networks.

For a Kagome network subject to uniaxial tension in the x-direction (0°), a similar elastic beam model can be used to estimate its effective mechanical properties. In this case, each horizontal fiber segment is subject to an axial tensile force and a bending moment, and each slanted segment is subject to a horizontal force and a bending moment at each end. For a low-density Kagome network ($\rho \ll 1$), the bending moments are approximately zero at all joints, and the axial force is approximately zero in all slanted segments, recovering the truss model with only the horizontal fibers carrying the load. The effective Poisson's ratio and Young's modulus are the same as in the y-direction, but the effective tensile strength in the x-direction is lower, $S_{eff} \approx \frac{1}{3}\rho S_f$, as opposed to $S_{eff} \approx \frac{1}{2}\rho S_f$ in the y-direction. However, for a low-density Kagome network ($\rho \ll 1$), fiber buckling could occur to lower the effective stiffness of the network in the y-direction (Mane et al., 2021), and thus the effective tensile strength in the y-direction can be considerably lower than that predicted by the truss model or the elastic beam model without considering the effect of fiber buckling.

In the limit of low relative density ($\rho \ll 1$), the effective mechanical properties (e.g., Young's modulus, Poisson's ratio, and tensile strength) predicted by the truss model are identical for the triangular and Kagome networks, as listed in Table 1. However, by the elastic beam model, the effects of bending are different for the two types of networks (Mane, 2023), and the critical conditions for onset of buckling are also different (Mane et al., 2021). The difference between the triangular and Kagome networks may be attributed to the difference in the joint or nodal connectivity (Fleck et al., 2010). Moreover, while there are two types of joints (SH and SS) in a Kagome network, all joints in a triangular network are of the same type (with same symmetry).

2.1. Fiber buckling in Kagome and triangular networks

For a Kagome or triangular network subject to uniaxial tension in the y-direction (Fig. 1), the fiber segments in the transverse direction are under compression, due to Poisson's effect with $\nu_{eff} \approx 1/3$. When the compressive force exceeds a critical value, the fiber segments buckle, leading to a nonlinear, elastic behavior of the network (Mane et al., 2021). The effective stress at the onset of fiber buckling may be considered as a limiting stress for the linearly elastic response of the Kagome/triangular network. The tensile strength predicted by the truss model or the elastic beam model is valid only if damage initiation occurs before onset of fiber buckling.

For a low-density triangular network ($\rho \ll 1$) subject to uniaxial tension in the y-direction, assuming that all joints are rigid and cannot rotate (due to symmetry), the effective stress for onset of fiber buckling is (Mane, 2023):

$$\sigma_B = \frac{\pi^2}{36}\rho^3 E_f. \tag{2.15}$$

For a low-density Kagome network ($\rho \ll 1$) subject to uniaxial tension in the y-direction, the effective stress for onset of buckling follows the same scaling, $\sigma_B \sim \rho^3 E_f$, but the coefficient is different, because the SH joints in the Kagome network can rotate (with an elastic resistance). Previously, by numerical simulations (Mane et al., 2021), we obtained the critical strain for onset of buckling as

$$\varepsilon_B = \frac{\beta}{\kappa^2}\rho^2, \tag{2.16}$$

where $\beta = 1/4$ and $\kappa = 0.55$ for a triangular network, and $\beta = 1$ and $\kappa = 0.72$ for a Kagome network. The corresponding effective stress is simply,

$$\sigma_B = E_{eff}\varepsilon_B \approx \frac{\beta}{3\kappa^2}\rho^3 E_f. \tag{2.17}$$

For a triangular network, a comparison between Eq. (2.15) and Eq. (2.17) leads to $\kappa = \sqrt{3}/\pi$, in close agreement with the numerical result ($\kappa = 0.55$). For a Kagome network, based on the numerical results, $\kappa =$

0.72, and thus the effective stress for onset of fiber buckling is: $\sigma_B \approx 0.643\rho^3 E_f$, which is considerably higher than the critical stress for the triangular network of the same relative density (by a factor of ~ 2.3).

Compare σ_B and S_{eff} for a low-density Kagome (or triangular) network ($\rho \ll 1$) subject to uniaxial tension in the y-direction. The former scales with $\rho^3 E_f$, while the latter scales approximately with ρS_f. The ratio between the two, σ_B/S_{eff}, scales with $\rho^2 E_f/S_f$. Thus, the dimensionless group, $\rho^2 E_f/S_f$, determines if the network fails before or after the onset of fiber buckling. If $\sigma_B/S_{eff} > 1$, fracture of the brittle fibers initiates before onset of buckling, which is the case of pre-buckling failure for a network with a relatively large value of $\rho^2 E_f/S_f$ (high relative density and low fiber strength). Otherwise, if $\sigma_B/S_{eff} < 1$, fiber buckling occurs before fracture, which is the case of post-buckling failure for a network with a relatively small value of $\rho^2 E_f/S_f$ (low relative density and high fiber strength). The effective tensile strength of the network due to the post-buckling failure cannot be predicted by the linear truss or beam model. Next we present a numerical method to simulate both the pre-buckling and post-buckling failure of Kagome networks.

3. Finite element method

Similar to a previous work (Mane et al., 2021), we use the second-order Timoshenko beam elements in ABAQUS to model the fibers. The fiber material is assumed to be linearly elastic and brittle, characterized by Young's modulus E_f, Poisson's ratio ν_f (=0.3), and a tensile strength S_f. In order to model the elastic-brittle behavior of the fibers, we use a combination of two options in ABAQUS: (a) Progressive Damage and Failure and (b) User Defined Field Variable. This approach requires definition of an elastic–plastic response of the material along with a damage initiation criterion followed by damage evolution. Here, the elastic-brittle behavior is modeled by setting the yield strength to be S_f under tension and the critical strain for damage initiation to be $\varepsilon_f = S_f/E_f$, so that the plastic strain is zero between yielding and damage initiation. The subsequent damage evolution is specified in a tabular manner to degrade Young's modulus of the damaged material, so that the local stress drops to nearly zero. We assume that the fiber fails under tension only and remains linearly elastic under compression. The user-defined field variable is employed to model the tension–compression asymmetry. In the Timoshenko beam elements, the local stress and strain are evaluated at the section points along each cross-section of the beam located at the integration points of each element. Thus, each section point follows the elastic-brittle behavior, with Young's modulus degraded upon damage initiation. Each beam element may be partly damaged when a subset of its section points are damaged but the other section points are not.

As an example, we demonstrate the damage model by simulating an elastic-brittle fiber subject to three-point bend (Fig. 3). Here, the fiber is simply supported at both ends, and a point force is applied in the transverse direction at the center section of the fiber. The cross-section of the fiber is square with a depth d, and the ratio between the depth and the fiber length is $d/L = 0.05$. The fiber is modeled with 80 s-order Timoshenko elements. Each element has two integration points, and the number of section points across the depth of the beam is varied from 11 to 81. The simulated force–displacement responses in Fig. 3 show that at least 41 section points are necessary for convergence and accuracy, in comparison with the analytical prediction. Upon damage initiation, the force drops to zero, as expected for an elastic-brittle material subject to three-point bend. The numerical results in Fig. 3 show that the initiation of failure is slightly delayed at $\delta/L = 0.034$ (with 41 or 81 section points), while the analytical solution predicts failure at $\delta/L = 0.033$. This delay is due to the fact that the damage initiation is determined by the maximum local stress and strain evaluated at the integration points, located slightly to the left or right of the node at the center section, while theoretically the maximum local stress and strain occur exactly at the center section. The difference between the local stresses at the center section and at the closest integration points can be reduced by reducing the element size at the center where the point force is applied, which would then improve the agreement between the numerical result and the analytical prediction.

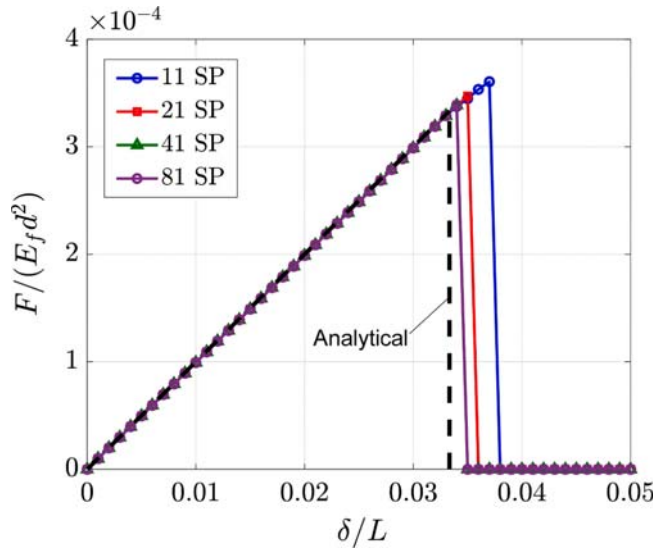

Fig. 3. Force-displacement response of an elastic-brittle fiber ($S_f/E_f = 0.01$) subject to three-point bend, using different numbers of section points (SP) in beam elements.

The finite element method with the damage model has been used for the study of the tensile strengths of periodic 2D networks, including Kagome, triangular and square networks (Mane, 2023). Implicit dynamic simulations are performed in ABAQUS, with Rayleigh stiffness proportional damping for stabilization. To minimize the dynamic effect, we apply sufficiently low strain rates so that the results are quasistatic with negligible kinetic energy. We caution that the damping coefficient (β) should be selected carefully, because a large damping coefficient could lead to inaccurate results. For the three-point bend problem, damping is not needed. Using damping with a small coefficient ($\beta = 10^{-4}$) gives similar numerical results, but the convergence is faster with damping in the simulation. However, using a larger damping coefficient would lead to a more progressive failure, uncharacteristic of the expected brittle failure, although the peak force corresponding to damage initiation is unaffected.

4. Unit cell model: Strength and failure modes

This section presents the numerical results for Kagome networks subject to uniaxial tension, based on the unit cell model (Fig. 1a) with periodic boundary conditions. The objective of the unit cell model is to determine the effective tensile strength for damage initiation and the corresponding failure modes.

Fig. 4 shows the simulated effective stress–strain behavior of the Kagome networks subject to uniaxial tension in the y-direction, with a relative density $\rho = 0.118$ and various values of the fiber strengths ($\varepsilon_f = S_f/E_f$). As shown previously in Mane et al. (2021), the stress–strain curve of the low-density Kagome network follow the linear response (the dashed line in Fig. 4) with an effective Young's modulus, $E_{eff} \approx \frac{1}{3}\rho E_f$, before onset of buckling. However, the effective stiffness of the network is significantly reduced after buckling. The critical strain for onset of buckling is approximately 0.027 for $\rho = 0.118$, as predicted by Eq. (2.16). If the fiber strength is low (e.g., $\varepsilon_f = 0.02$), damage initiation occurs before onset of buckling, upon which the effective stress drops to nearly zero. In this case, the effective strength of the network may be estimated by the elastic beam model, $S_{eff} \approx \frac{1}{2}\rho S_f(1-\rho)$ in Eq. (2.14). In

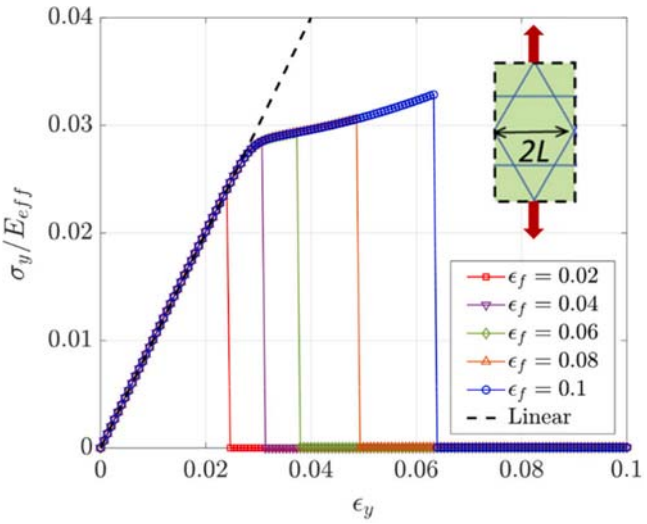

Fig. 4. Effective stress–strain curves of Kagome networks ($\rho = 0.118$) subject to uniaxial tension in the y-direction, for various values of the fiber strength ($\varepsilon_f = S_f/E_f$). The inset shows the unit cell and the direction of uniaxial tension.

contrast, if the fiber strength is high (e.g., $\varepsilon_f = 0.1$), damage initiation occurs after buckling. In this case, the effective strength of the Kagome network is much lower than the prediction of the elastic beam model, and the stress–strain curve resembles an elastic–plastic behavior, with a "yield strength" corresponding to the onset of buckling and an "ultimate" tensile strength corresponding to damage initiation.

While the linearly elastic behavior of the Kagome network is isotropic, the nonlinearly elastic behavior is anisotropic (Mane et al., 2021). Moreover, the linear beam or truss model predicts that the tensile strength is also anisotropic, lower in the x-direction compared to the y-direction (Table 1). Fig. 5a shows the simulated effective stress–strain behavior of Kagome networks subject to uniaxial tension in the x-direction, with a relative density $\rho = 0.118$ and various values of the fiber strengths. In all cases, the effective stress–strain response closely follows the linearly elastic behavior before damage initiation, slightly softer as the strain increases, due to geometric nonlinearity in the finite element model. Upon damage initiation, the effective stress drops to a very small value, compared to the maximum stress. Remarkably, after damage initiation, the effective stress of the network is not necessarily zero in

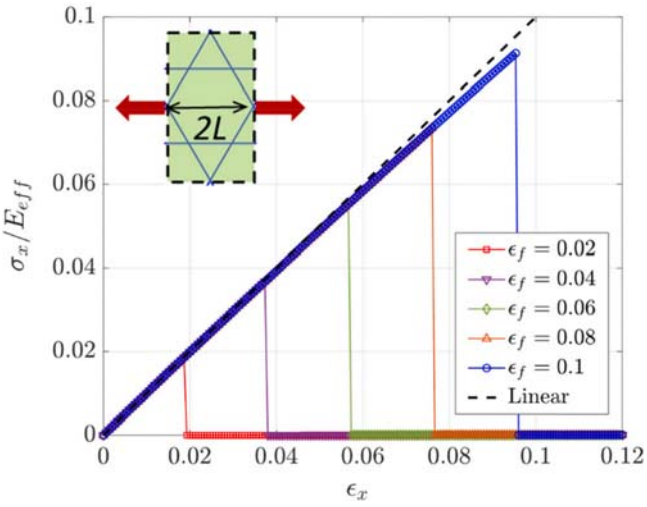

Fig. 5. Effective stress–strain curves of Kagome networks ($\rho = 0.118$) subject to uniaxial tension in the x-direction, for various values of the fiber strength ($\varepsilon_f = S_f/E_f$). The inset shows the unit cell and the direction of uniaxial tension.

this case. It is found that, before damage initiation, the fibers parallel to the x-direction are primarily under tension, while the stress is much lower in the slanted fibers. As a result, the fibers parallel to the x-direction are damaged first, and subsequently the unit cell of the Kagome network is degraded to a unit cell of a diamond network with only the slanted fibers that remain intact and connected. The fiber deformation in the unit cell of the diamond network is bending dominated and much more compliant so that the effective stress is much lower after damage initiation. However, it should be noted that, after the first damage initiation, the progression of damage in Kagome networks with many unit cells usually cannot be predicted by the unit-cell model. Nevertheless, the effective strengths of the Kagome networks are determined by the first damage initiation and thus can be predicted by the unit-cell model.

The effective tensile strengths of the Kagome networks are predicted by the maximum tensile stress in the effective stress–strain curves from the finite element simulations, corresponding to the first damage initiation in the unit cell model. Fig. 6(a and b) shows the effective strength as a function of the relative density for the Kagome networks subject to uniaxial tension in the x and y directions, respectively. For uniaxial tension in the x-direction, the effective strength follows the linear scaling with respect to the relative density, $S_{eff} \approx \frac{1}{3}\rho S_f$, as predicted by the elastic beam model. For all values of the fiber strength considered ($0.01 \le \varepsilon_f \le 0.1$), the ratio S_{eff}/S_f collapses onto the same line in Fig. 6 (a). In contrast, for uniaxial tension in the y-direction, the effective strength does not follow the linear scaling, and the ratio S_{eff}/S_f does not collapse onto the same line in Fig. 6(b). While the elastic beam model predicts a higher strength in the y-direction, $S_{eff} \approx \frac{1}{2}\rho S_f$, the prediction does not consider the nonlinearly elastic behavior due to buckling and thus generally overestimates the tensile strength in the y-direction. The elastic beam model without buckling is valid only if the damage initiation occurs before onset of buckling, that is, when the fiber strength is low (e.g., $\varepsilon_f = 0.01$) and the relative density of the network is high (e.g., $\rho = 0.118$). For a higher fiber strength or a lower relative density, the tensile strength of the Kagome network in the y-direction is significantly lower than the linear prediction. As noted in Mane et al. (2021), the elastic deformation of the Kagome networks is stretch-dominated before onset of buckling, but becomes bending-dominated after buckling, and transitions back to stretch-dominated at large strains. The transitions in the deformation mode lead to different scaling for the tensile strength, $S_{eff}/S_f\ \rho$ for the stretch-dominated deformation and $S_{eff}/S_f\ \rho^2$ for the bending-dominated deformation. Fig. 6(b) shows that, for the case of a low fiber strength (e.g., $\varepsilon_f = 0.01$), the effective tensile strength of the Kagome network follows the linear scaling at high relative densities, but transitions to the quadratic scaling at low densities. This transition corresponds to the transition from the stretch-dominated deformation before buckling (high density and small strain) to the bending-dominated deformation after buckling (low density and small strain). For the case of a high fiber strength (e.g., $\varepsilon_f = 0.1$), the effective tensile strength follows the quadratic scaling at high relative densities, but transitions to the linear scaling at low densities. This transition appears opposite to the case of a low fiber strength, and corresponds to the transition from the bending-dominated deformation after buckling (high density and large strain) to the stretch-dominated deformation at large strains (low density and large strain).

Next we examine the failure modes of Kagome networks. Fig. 7 shows the simulated deformations of a Kagome network subject to uniaxial tension in the x-direction. The color contour shows the beam stress in the fibers. Before damage initiation (Fig. 7a), the horizontal fibers are under tension, while the slanted fibers are bent slightly with a much smaller stress magnitude. All fibers deform elastically until the maximum tensile stress in the horizontal fibers reaches the fiber strength S_f, at $\varepsilon_x \approx 0.057$. This strain is slightly below $\varepsilon_f = 0.06$, because the local strain in the horizontal fibers near the SH joints is slightly higher than the applied strain ε_x, due to a small bending deformation. As a

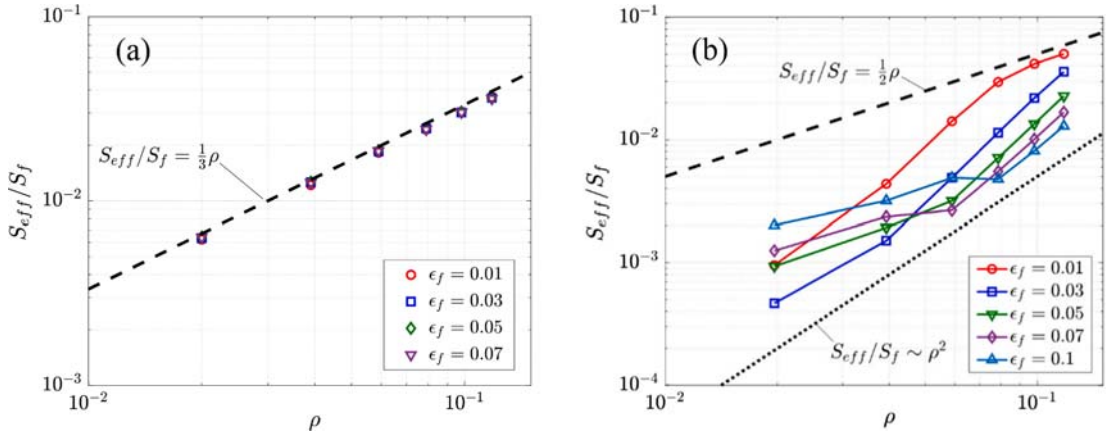

Fig. 6. Effective tensile strength of the Kagome network predicted by the finite element simulations, subject to uniaxial tension (a) in the x direction and (b) in the y direction. The dashed lines show the linear scaling, and the dotted line in (b) shows the quadratic scaling.

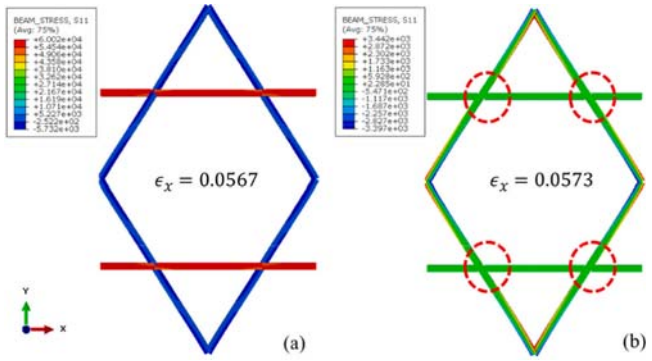

Fig. 7. Deformation and failure of a Kagome network ($\rho = 0.118$ and $\varepsilon_f = 0.06$), subject to uniaxial tension in the x-direction. (a) $\varepsilon_x = 0.0567$, before damage initiation; (b) $\varepsilon_x = 0.0573$, immediately after damage initiation near the SH joints (circled). The color contours show the beam stress in the fibers.

result, damage initiation occurs in the horizontal fibers near the SH joints circled in Fig. 7(b). Upon damage initiation, the horizontal fibers are compromised due to brittle failure, but the slanted fibers remain intact so that the network retains connectivity. Thus, when the Kagome network is subject to uniaxial tension in the x-direction, the primary failure mode is the brittle fracture of the horizontal fibers, same for all relative densities and fiber strength values considered. Therefore, the effective tensile strength of the low-density Kagome network in the x-direction can be predicted reasonably well by the elastic beam model, $S_{eff} \approx \frac{1}{3}\rho S_f$, as shown in Fig. 6(a). We note that the simpler truss model predicts a uniform tensile stress in the horizontal fibers before damage initiation, and thus cannot predict the location of damage initiation. Both the elastic beam model and the finite element simulations predict that the damage initiation occurs in the horizontal fibers near the SH joints, due to the small bending deformation of the fibers near the SH joints.

Several different failure modes are predicted for the Kagome networks subject to uniaxial tension in the y-direction. Corresponding to the effective stress–strain curves in Fig. 4, there are two failure modes for the Kagome networks with $\rho = 0.118$, as shown in Fig. 8. For the case of a low fiber strength ($\varepsilon_f = 0.01$), damage initiation occurs before onset of buckling (Fig. 8a–b). As predicted by the elastic beam model, the slanted fibers are under tension (red) and the horizontal fibers under compression (blue) before damage initiation. The local tensile stress is the highest near the SS joints between two slanted fibers. When the local tensile stress reaches the fiber strength, damage initiation occurs in the slanted fibers near the SS joints, and the effective stress of the network drops to nearly zero. This is a case of pre-buckling failure ($S_{eff} < \sigma_B$), which is expected for the Kagome network of a relatively high density and low fiber strength. The effective tensile strength for this failure mode can be well predicted by the elastic beam model without buckling, namely, $S_{eff} \approx \frac{1}{2}(1-\rho)\rho S_f$ by Eq. (2.14).

For the Kagome network with $\rho = 0.118$ and a higher fiber strength ($\varepsilon_f = 0.06$), the higher fiber strength allows the horizontal fibers to buckle before damage initiation (Fig. 8c–d). After buckling, the location of the highest local stress in the fibers changes from the SS joints to the SH joints. The bending deformation becomes significant near the SH joints due to buckling of the horizontal fibers, causing higher tensile stress in the slanted fibers near these joints. Upon damage initiation, the

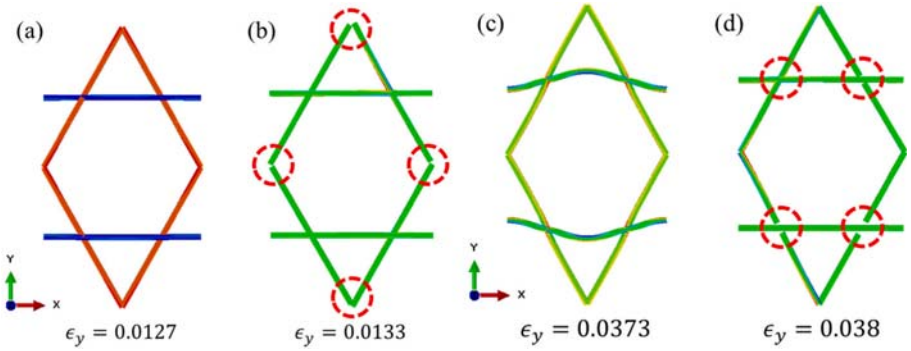

Fig. 8. Failure modes of a Kagome network ($\rho = 0.118$) subject to uniaxial tension in the y-direction. (a-b) Pre-buckling failure for $\varepsilon_f = 0.01$, before and after damage initiation near the SS joints (circled). (c-d) Post-buckling failure for $\varepsilon_f = 0.06$, before and after damage initiation near the SH joints (circled). The color contours show the beam stress in the fibers.

slanted fibers fail completely at the SH joints, and the effective stress of the network drops to nearly zero (Fig. 4). This is a case of post-buckling failure ($S_{eff} > \sigma_B$), which is expected for the Kagome network of a relatively high fiber strength. The effective tensile strength for this failure mode can be considerably lower than that predicted by the linear beam model (Fig. 6b).

In addition, two other failure modes are predicted for Kagome networks with a lower relative density, subject to uniaxial tension in the y-direction. Fig. 9a shows the effective stress–strain curves for the Kagome networks with a relative density $\rho = 0.079$. Similar to Fig. 4, the effective stress drops to nearly zero before onset of buckling when the fiber strength is low ($\varepsilon_f = 0.01$), indicating the pre-buckling failure near the SS joints, similar to that shown in Fig. 8(a–b). For $\varepsilon_f = 0.04$, the effective stress drops to nearly zero after buckling, indicating the post-buckling failure near the SH joints, similar to that shown in Fig. 8 (c–d). However, for $\varepsilon_f = 0.07$ and 0.1, the effective stress first drops to an intermediate level, followed by an increase and a second drop. This type of stress–strain behavior results from a different failure mode shown in Fig. 9(b–e). Fig. 9(b) shows the deformation of the Kagome network with $\rho = 0.079$ and $\varepsilon_f = 0.07$ before damage initiation, with significant buckling of the horizontal fiber segments. In this case, the location of the highest tensile stress in the fibers shifts to the center of the buckled fiber segments, where the bending curvature is the largest. While the horizontal segments are under compression overall, significant bending due to buckling induces a high tensile stress locally at the crest, surpassing the tensile stress in the slanted fibers. Consequently, the first damage initiation occurs in the horizontal fiber segments near the center (away from the joints). Interestingly, this damage initiation does not lead to complete failure of the horizontal fiber segments. As shown in Fig. 9(c), the horizontal fibers remain connected, but the local stress is reduced at the center, indicating partial failure of the horizontal fibers. As a result, the effective stress of the network drops, but not as much as it would if the horizontal fibers were fully damaged. The partial failure of the buckled fiber segments may be understood as a result of the overall compression of the horizontal fibers, stabilizing damage evolution under the displacement-controlled loading. Subsequently, the Kagome network becomes more compliant but remains connected with partially damaged horizontal fibers (Fig. 9d). The location of the highest local stress now shifts back to the slanted fibers near the SH joints, where the second damage initiation occurs (Fig. 9e). The effective stress drops to nearly zero upon the second damage initiation, when the slanted fibers fail near the SH joints, leading to complete loss of the network connectivity. Again, it is noted that, after the first damage initiation, the progression of damage in Kagome networks with many unit cells cannot be predicted by the unit-cell model. In this case, the effective tensile strength of the Kagome network is associated with the first damage initiation due to post-buckling failure of the horizontal segments. The deformation just before the first damage initiation is elastic and bending dominated, and thus the effective tensile strength of the network follows the quadratic scaling ($S_{eff}/S_f \sim \rho^2$) as shown in Fig. 6(b).

Yet another mode of failure is predicted for the cases of the lowest relative density considered ($\rho = 0.02$), with the two highest fiber strengths ($\varepsilon_f = 0.09$ and 0.1) considered. As shown in Fig. 10(a), the effective stress–strain curve for such a low-density Kagome network is linear only at very small strains, with a small critical strain (~0.002) for the onset of buckling. Thus, the pre-buckling failure is unlikely in this case. After buckling, the effective stress–strain curve of the network is nearly flat at small strains but stiffens significantly at large strains, as the fiber deformation transitions from bending-dominated to stretch-dominated. Such a nonlinear and elastic behavior is similar to strain stiffening in polymer networks (Boyce and Arruda, 2000). When the fiber strength is low ($\varepsilon_f < 0.09$), post-buckling failure of the horizontal segments occurs first, followed by failure of the slanted segments near the SH joints, similar to Fig. 9(b–e). When the fiber strength is high ($\varepsilon_f = 0.09$ and 0.1), however, the tensile stress in the buckled fiber segments is insufficient to cause damage initiation. Instead, significant stiffening occurs as the slanted fibers rotate to align with the loading direction. Although the horizontal fiber segments are buckled with significant bending deformation, the overall deformation of the network becomes stretch-dominated, and the location of the maximum tensile stress shifts back to the slanted fibers near the SS joints (Fig. 10b). Consequently, damage initiation occurs near the SS joints (Fig. 10c), and the effective stress of the network drops to nearly zero upon damage initiation. While the location of damage initiation in this case is the same as the pre-buckling failure mode (Fig. 8b), we note that the post-buckling failure near the SS joints cannot be predicted by the linear beam or truss mode. The corresponding tensile strength is much lower than the prediction of the elastic beam model (see Fig. 6b), and the effective strain at failure is much larger. Thus, with significant buckling of the horizontal fiber segments, the low-density Kagome network is very stretchable, similar to a diamond network (as if the horizontal fibers do not exist).

The four different failure modes of the Kagome networks subject to uniaxial tension in the y-direction are summarized in a phase diagram (Fig. 11), in the plane of the relative density ρ and the normalized fiber strength ($\varepsilon_f = S_f/E_f$), where different failure modes from the numerical simulations are marked by different symbols in four regions (A-D). We emphasize that these failure modes refer only to the first damage initiation predicted by the unit-cell model. The boundary between the pre-buckling failure (Region A) and the post-buckling failure (Regions B-D) can be determined from Eq. (2.16), which predicts a critical strain for onset of buckling, $\varepsilon_B \sim \rho^2$. Before onset of buckling, the local stress in the fiber is linearly proportional to the effective strain applied to the network. Thus, the highest fiber strength for the pre-buckling failure is

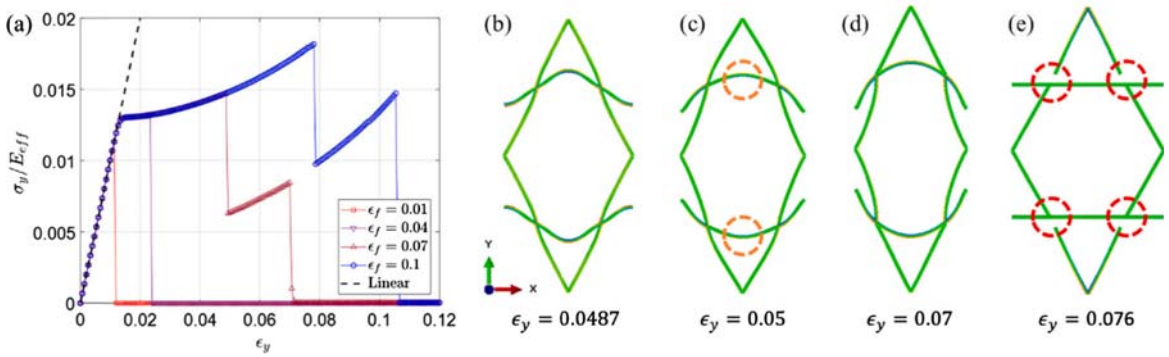

Fig. 9. (a) Effective stress–strain curves of Kagome networks ($\rho = 0.079$) subject to uniaxial tension in the y-direction, with various values of the fiber strength. (b-e) Post-buckling failure of the horizontal segments and then SH joints in a Kagome network ($\rho = 0.079, \varepsilon_f = 0.07$), subject to uniaxial tension in the y-direction: (b) before the first damage initiation; (c) immediately after the first damage initiation, with partial damage in the buckled fiber segments (circled); (d) before the second damage initiation; and (e) after the second damage initiation at SH joints (circled). The color contours show the beam stress in the fibers.

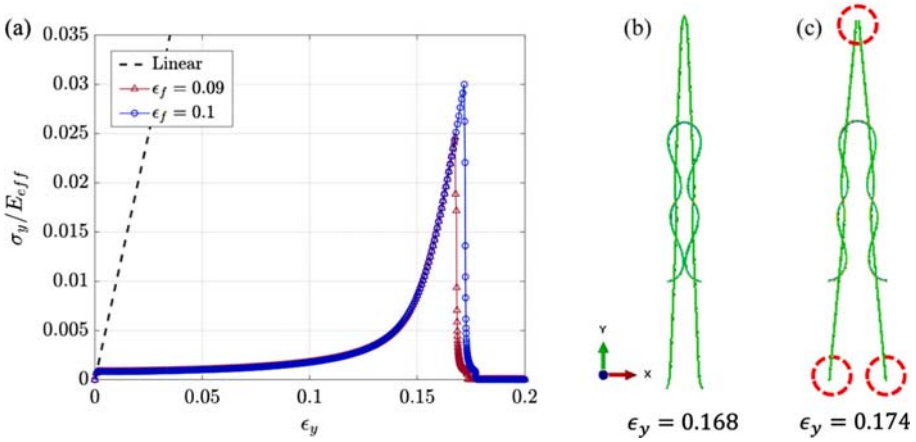

Fig. 10. (a) Effective stress–strain curves of Kagome networks of a low relative density ($\rho = 0.02$) and high fiber strengths ($\varepsilon_f = 0.09$ and 0.1), subject to uniaxial tension in the *y*-direction. (b-c) Post-buckling failure of the Kagome network ($\rho = 0.02, \varepsilon_f = 0.09$), before and after damage initiation at the SS joints (circled), showing only the upper half of the unit cell.(The finite element model did not account for possible contact between the fibers. However, in this case, the horizontal fiber segments are buckled so much that they contact and cross the slanted fibers.).

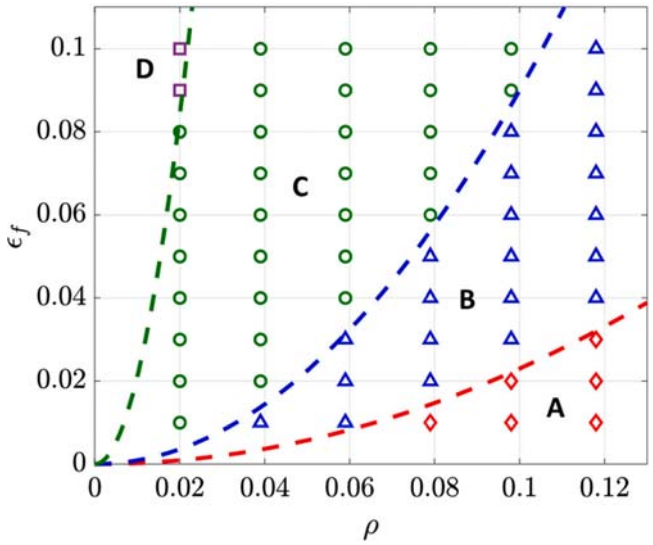

Fig. 11. A phase diagram of failure modes in Kagome networks, subject to uniaxial tension in the *y*-direction. Region A (diamonds): pre-buckling failure near SS joints; Region B (triangles): post-buckling failure near SH joints; Region C (circles): post-buckling failure of horizontal segments; Region D (squares): post-buckling failure near SS joints.

proportional to the buckling strain ($\varepsilon_B \sim \rho^2$) and scales with the relative density quadratically shown as the red dashed line in Fig. 11. Interestingly, the same scaling appears to be valid for the boundaries between the three post-buckling failure modes, shown as the blue and green dashed lines in Fig. 11, although the boundary between Regions C and D may not be well defined with only two data points in Region D. Evidently, a low-density Kagome network is likely to fail by one of the post-buckling modes, so that the effective tensile strength in the *y*-direction is lower than the prediction of the elastic beam or truss model. A similar phase diagram of the failure modes has been constructed for the triangular networks (Mane, 2023).

5. Effect of boundary conditions

In this section we study the effect of boundary conditions on the tensile strength of Kagome networks consisting of a large number of unit cells. In particular, we consider rectangular panels made from Kagome networks, as in typical experiments for measuring mechanical properties (Gu et al., 2018; Luan et al., 2022). Since the effective Poisson's ratio of a Kagome network is 1/3 in the linear regime and becomes much larger after buckling under uniaxial tension in the *y*-direction (Mane et al., 2021), the mechanical behavior of the Kagome network can be sensitive to the boundary conditions.

5.1. Periodic boundary condition

First consider Kagome networks of different sizes, subject to uniaxial tension in the y direction under periodic boundary conditions. We simulate the deformation and failure of these networks by the same finite element method as for the unit-cell model in Section 4. In a previous study (Mane et al., 2021), we have shown that, for a perfect Kagome network, buckling occurs simultaneously in all unit cells, and the post-buckling elastic deformation remains periodic. Thus, we expect that damage initiation under the periodic boundary condition remains the same as that in the unit-cell model. Indeed, the effective stress–strain responses under the periodic boundary conditions are similar to those predicted by the unit-cell model (e.g., Fig. 4). In particular, the effective tensile strength associated with the first damage initiation is nearly identical to that predicted by the unit-cell model (Fig. 6b), independent of the network size. However, after damage initiation, the stress–strain responses are somewhat different for different network sizes (Mane, 2023), indicating potentially different damage progression in the Kagome networks after damage initiation. In the present study, we consider only perfect Kagome networks in numerical simulations under the periodic boundary condition. The fact that not all unit cells are damaged simultaneously in a perfectly periodic Kagome network can only be attributed to some inevitable numerical noises in the simulations. In reality, with flaws or imperfections in the Kagome networks, such heterogeneous damage initiation commonly occurs, which, however, is beyond the scope of the present study. By considering only perfect Kagome networks under the periodic boundary conditions, our focus here is on the effective tensile strength associated with damage initiation, not so much about damage propagation.

5.2. Roller boundary condition

Next, we apply a roller boundary condition to the upper and lower edges of the Kagome network (Fig. 12a), while leaving the two vertical edges free. The vertical displacement is zero at the lower edge, and a constant vertical displacement is imposed to the upper edge, stretching the network in the y-direction. The roller boundary condition allows

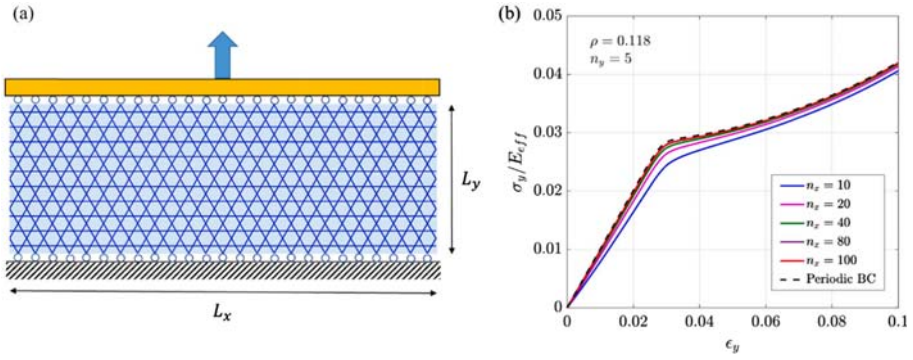

Fig. 12. (a) A Kagome network subject to uniaxial tension in the y-direction under the roller boundary condition. (b) Effective elastic stress–strain curves for Kagome networks ($\rho = 0.118$ and $n_y = 5$) of various sizes (n_x), subject to uniaxial tension in the y-direction with the roller boundary condition.

lateral contraction in the x-direction due to Poisson's effect, with no restriction on the horizontal displacement or rotation at the edges. The free vertical edges resemble free surfaces of a finite body. By symmetry, only one half of the network is simulated in the finite element model, with a symmetry boundary condition along the vertical center line.

Fig. 12(b) shows the effective stress–strain curves for Kagome networks ($\rho = 0.118$) with the roller boundary condition. The size of the network is varied by the number of unit cells in the x-direction (n_x), while the number of unit cells in the y-direction is fixed ($n_y = 5$). The nominal strain of the network in the y-direction is related to the vertical displacement imposed at the upper edge, $\varepsilon_y = u_y/L_y$, where $L_y = 2\sqrt{3}Ln_y$. The effective nominal stress is calculated from the reaction forces, $\sigma_y = F_y/(L_x d)$, where $L_x = 2Ln_x$ and F_y is the sum of all reaction forces in the y direction along the upper edge. Compared to the elastic response under the periodic boundary condition, the elastic response is more compliant under the roller boundary condition, and is dependent on the network size (n_x). As n_x increases, the network becomes stiffer, and approaches the elastic stress–strain response under the periodic boundary condition when $n_x > 40$. This result resembles the surface effect in crystals and edge effects in 2D crystals such as graphene (Lu et al., 2011). Evidently, the network is locally more compliant near the free edges, so that the overall response of the Kagome network is more compliant under the roller boundary condition with two free edges. As n_x increases, the fraction of the network near the free edges decreases, and the edge effect diminishes. Similar edge effects were noted by Fleck and Qiu (2007), indicating the presence of a boundary layer at the free edge of a Kagome network subject to either tension or shear loading.

To investigate the inelastic responses of Kagome networks under the roller boundary condition, we select a relatively large network model with $n_x = 100$ and $n_y = 5$ so that the edge effect on the elastic response is negligible. Fig. 13(a) shows the effective stress–strain responses of the Kagome networks with various tensile strengths of the fiber ($\varepsilon_f = S_f/E_f$). When ε_f is relatively large (>0.04), the stress–strain response is similar to that under the periodic boundary condition (Fig. 4). However, for $\varepsilon_f = 0.02$, the effective stress–strain response under the roller boundary condition appears different than that under the periodic boundary condition. Here, damage initiation occurs earlier as the stress–strain response deviates from linear elasticity, but the effective stress continues to increase after damage initiation, reaching a peak and then decreasing. Such a stress–strain response indicates a progressive damage process (Fig. 14).

Fig. 14(a) shows a "diffusive" damage progression in a Kagome network ($\rho = 0.118$, $\varepsilon_f = 0.02$, $n_x = 100$, $n_y = 5$) under the roller boundary condition, where the damage process starts at the free edge and gradually "diffuse" inwards as the applied nominal strain ε_y increases. At $\varepsilon_y = 0.00933$, the network is elastic, with no damage in any fiber segments. The axial force is nearly uniform in all slanted fiber segments except for those near the free edge, where the axial force is lower. The horizontal fibers are mostly straight without buckling, but with some bending deformation near the free edge. At $\varepsilon_y = 0.0167$, damage initiation first occurs near the upper and lower corners of the free edge, and the axial force is reduced in a layer of fiber segments near the free edge. The distribution of the axial force in the fibers reflects the damage progression. As the nominal strain increases, damage progresses

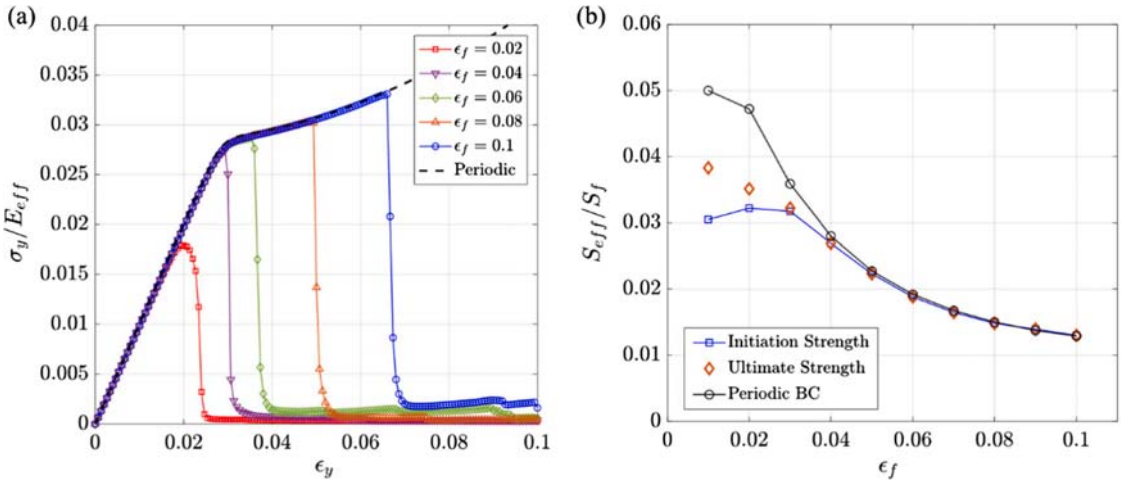

Fig. 13. (a) Effective stress–strain curves of Kagome networks subjected to tension in the y-direction under the roller boundary condition ($\rho = 0.118, n_x = 100, n_y = 5$), with various tensile strengths of the fiber. (b) Normalized damage initiation and ultimate tensile strengths of the Kagome networks ($\rho = 0.118$) under the roller boundary condition, in comparison with the effective tensile strength under the periodic boundary condition.

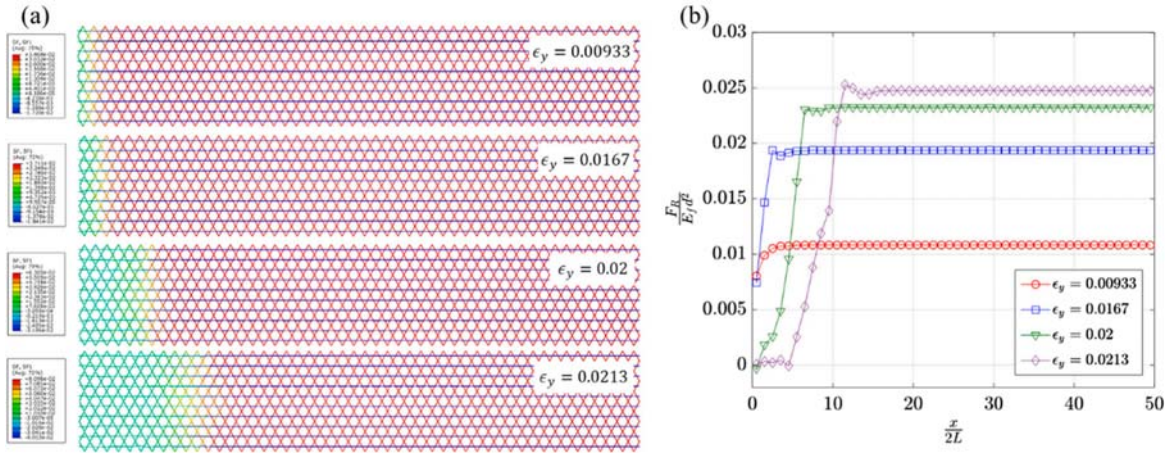

Fig. 14. (a) Damage progression in a Kagome network under the roller boundary condition ($\varepsilon_f = 0.02, \rho = 0.118, n_x = 100, n_y = 5$), with color contours of axial force in the fibers. (b) Normalized reaction force along the upper edge of the Kagome network.

inward from the free edge, and the axial force is reduced in an increasingly thicker layer of fiber segments, resembling a diffusion process. Such a diffusive damage progression can also be shown by the reaction forces along the upper boundary of the Kagome network (Fig. 14b). At $\varepsilon_y = 0.00933$, the reaction force is a constant except for a transition region toward the free edge, where the reaction force is lower. At $\varepsilon_y = 0.0167$, the reaction force drops slightly at the joint closest to the free edge, but increases elsewhere. Thus, damage initiation in this case is localized near the free edge, and the overall effective stress of the network continues to increase with the nominal strain ε_y. This is in contrast with the abrupt drop of the effective stress upon damage initiation in the same Kagome network ($\varepsilon_f = 0.02$) under the periodic boundary condition (Fig. 4). The effective stress continues increasing till $\varepsilon_y = 0.02$, at which point the reaction force drops to nearly zero at the joint closest to the free edge, and the transition region has expanded further inward. As the nominal strain increases further, a damage region emerges near the free edge with nearly zero reaction forces. As the damage region expands, the effective stress decreases, despite that the reaction force continues to increase in the undamaged region away from the free edge. Eventually, at $\varepsilon_y \approx 0.025$, the entire network is consumed by the damage region, and the effective stress drops to nearly zero (Fig. 13a).

For the case of a relatively high fiber strength ($\varepsilon_f > 0.04$), we observe different damage initiation and progression under the roller boundary condition, as shown in Fig. 15 for $\varepsilon_f = 0.1$. Here, damage initiation occurs after buckling of the horizontal fibers, and the effective stress drops sharply upon damage initiation. Although the network is more compliant near the free edge with more bending deformation, damage initiation occurs simultaneously throughout the entire network at $\varepsilon_y = 0.066$, similar to the case under the periodic boundary condition. However, the corresponding failure mode is different. Under the periodic boundary condition, the post-buckling failure would occur in the slanted segments near the SH joints (Region B in Fig. 11). Under the roller boundary condition, our simulation shows that damage initiation occurs in the buckled horizontal segments with partial damage (Fig. 15a). Subsequently, a periodic deformation pattern emerges at $\varepsilon_y = 0.0667$ (Fig. 15b), with localized shear deformation along the boundaries between triangular and diamond shaped "domains". Meanwhile, the damaged network contracts significantly in the *x*-direction. After buckling and partial damage of the horizontal fibers, the Kagome network becomes more compliant, with a low resistance to shear along the diagonal directions, similar to a diamond-celled lattice (Quintana Alonso and Fleck, 2009). Consequently, the homogeneous deformation becomes unstable and gives way to inhomogeneous, localized shear deformation, resembling shear bands in metals (Needleman and Tvergaard, 1992).

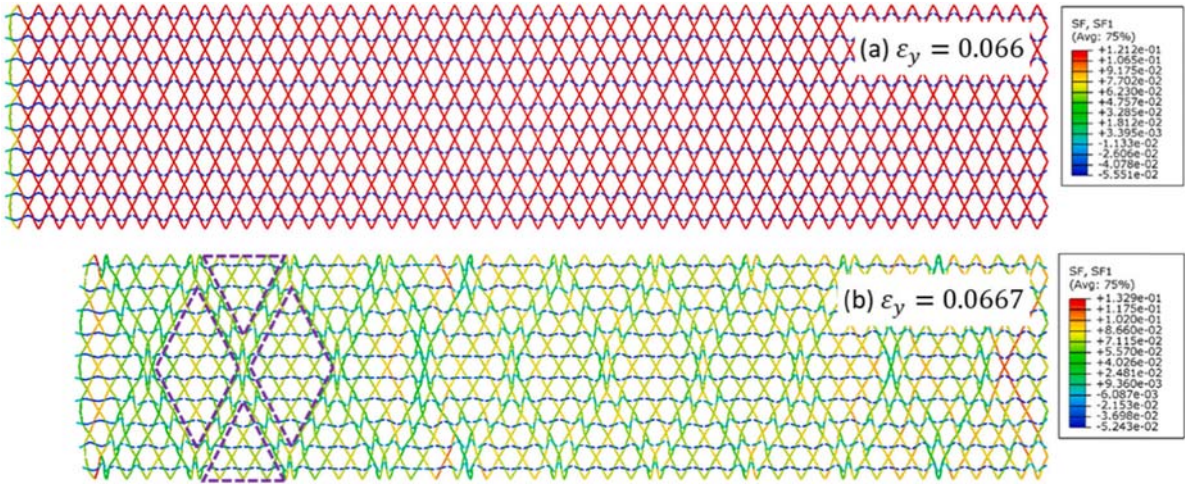

Fig. 15. Deformation and damage in a Kagome network under the roller boundary condition ($\varepsilon_f = 0.1, \rho = 0.118, n_x = 100, n_y = 5$), with color contours showing the axial force in the fibers. (a) $\varepsilon_y = 0.066$, immediately after damage initiation, and (b) $\varepsilon_y = 0.0667$, with localized shear deformation between triangular and diamond shaped "grains" (illustrated by the dash-lined shapes).

The effective tensile strengths of the Kagome networks under the roller boundary condition are compared with those under the periodic boundary condition in Fig. 13(b). For a relatively low fiber strength ($\varepsilon_f < 0.04$), the initiation and ultimate tensile strengths are different, and both are considerably lower than those under the periodic boundary condition. As shown in Fig. 14, the lower strength in this case is due to damage initiation near the free edges, followed by a diffusive damage progression. In contrast, for a relatively high fiber strength ($\varepsilon_f \geq 0.04$), the initiation and ultimate tensile strengths are nearly identical and compare closely with those under the periodic boundary condition. In this case, the presence of free edges does not influence the effective strength of the network, and damage initiation occurs spontaneously throughout the network (Fig. 15). Incidentally, the transition from the edge-induced diffusive damage to the edge-independent spontaneous damage under the roller boundary condition coincides with the transition from the pre-buckling failure to the post-buckling failure under the periodic boundary condition as shown in Fig. 11 for $\rho = 0.118$.

5.3. Clamped boundary condition

A more realistic model close to common experimental conditions is to have the upper and lower edges of the Kagome network clamped (Fig. 16a), while leaving the two vertical edges free. In this case, both the vertical and horizontal displacements as well as the rotations are restricted to be zero along the lower edge, and a constant vertical displacement is imposed on the upper edge along with zero horizontal displacement and zero rotation. As a result, lateral contraction of the Kagome network is restricted except for the regions near the free edges. By symmetry, only one half of the network is simulated in the finite element model, with a symmetry boundary condition along the vertical center line.

Fig. 16(b) shows the effective elastic response of Kagome networks with the clamped boundary condition, for the relative density $\rho = 0.118$ and different network sizes. Unlike the periodic or the roller boundary condition, the Kagome networks under the clamped boundary condition exhibit nearly linear effective stress–strain behaviors, with no sign of buckling. For a sufficiently large n_x ($\gg n_y$), most part of the network is subject to a biaxial tension with zero strain in the x direction ($\varepsilon_x = 0$), due to the constraint imposed by the clamped boundary condition along the upper and lower edges. In this case, the horizontal fibers are not under compression and thus do not buckle. With the effective Young's modulus $E_{eff} \approx \frac{1}{3}\rho E_f$ and the effective Poisson's ratio $\nu_{eff} \approx \frac{1}{3}$, the apparent stiffness for a large Kagome network with the clamped boundary condition can be predicted as: $\overline{E}_{app} = \frac{E_{eff}}{1-\nu_{eff}^2} = \frac{9}{8}E_{eff}$, which is slightly stiffer than the same network under the periodic boundary condition. As shown in Fig. 16(b), for $n_x = 100$ and $n_y = 5$, the apparent stiffness is close to $\overline{E}_{app}$ (which is the theoretical limit for $n_x \to \infty$). For a smaller n_x, the network is more compliant, due to the presence of the free edges.

Fig. 17 shows the deformation of a Kagome network of size $n_x = 40$, $n_y = 5$ and a relative density $\rho = 0.118$, under the clamped boundary condition. It can be seen in Fig. 17(a) that the strain energy density is lower in the fibers near the free edge, although locally higher near some joints. At a higher nominal strain ($\varepsilon_y = 0.1$), the network contracts laterally in the middle but remains constrained at the upper and lower edges by the clamped boundary condition (Fig. 17b). Such a deformation is similar to a thin membrane in a pure shear test (Rivlin and Thomas, 1953). As a result, the deformation in the network is inhomogeneous, with more bending near the free edge. Away from the free edge, the deformation of the network is nearly homogeneous. The horizontal fibers are buckled only in the region near the free edge, and remain straight elsewhere. Notably, the highest strain energy density appears in the fiber segments close to the upper/lower corners of the free edge, where damage initiation is likely to occur.

Fig. 18(a) shows the effective stress–strain responses of the Kagome networks of size ($n_x = 60, n_y = 5$) with various fiber strengths, under the

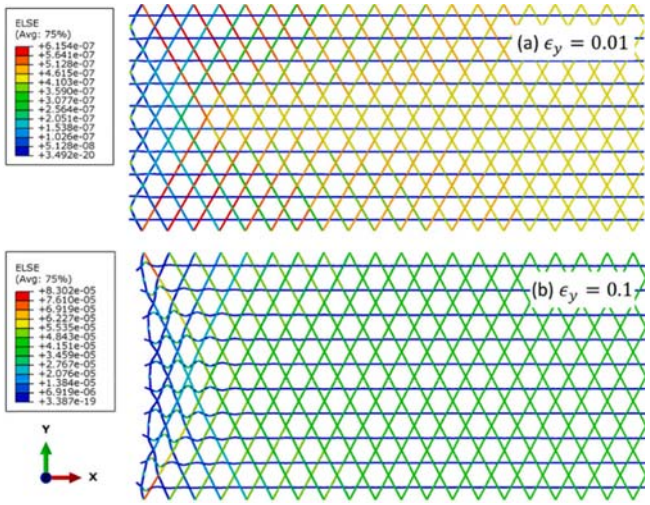

Fig. 17. Deformed Kagome network (half model) under the clamped boundary condition ($\rho = 0.118, n_x = 40, n_y = 5$). (a) $\varepsilon_y = 0.01$ and (b) $\varepsilon_y = 0.1$, with color contours showing the strain energy density in the fibers.

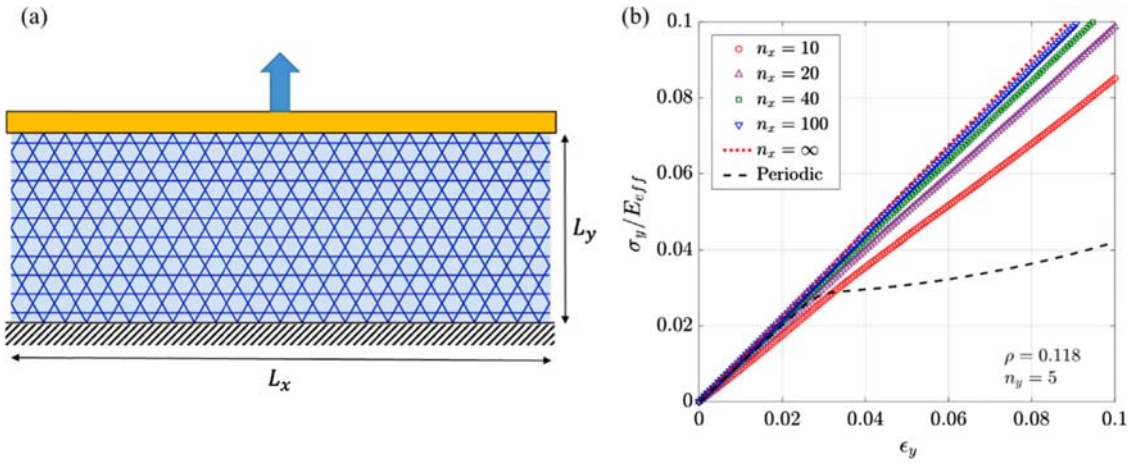

Fig. 16. (a) A Kagome network subject to uniaxial tension in the y-direction under the clamped boundary condition. (b) Effective elastic stress–strain curves for the Kagome networks with the clamped boundary condition ($\rho = 0.118, n_y = 5$), for various network sizes (n_x).

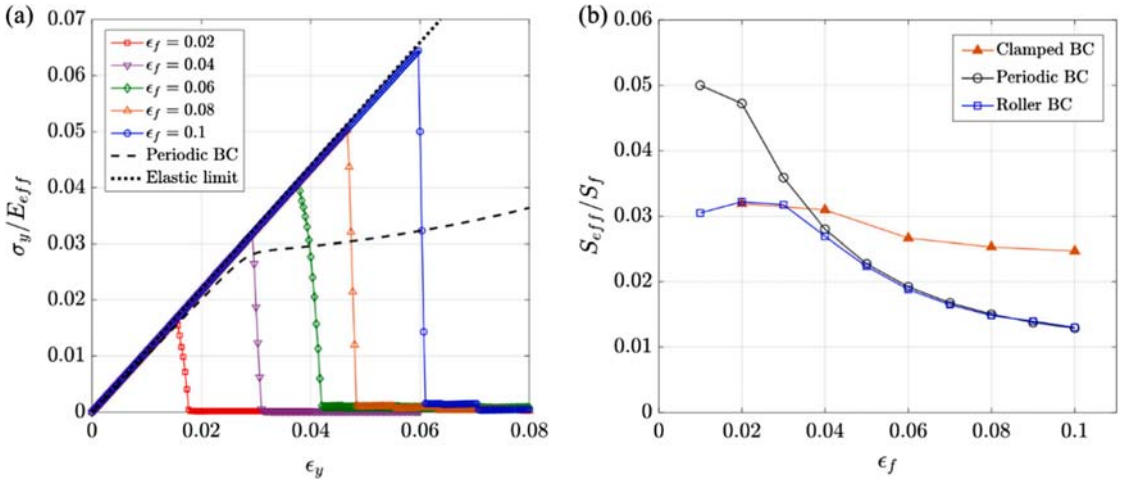

Fig. 18. (a) Effective stress–strain curves of Kagome networks with the clamped boundary condition ($\rho = 0.118, n_x = 60, n_y = 5$), with various fiber strengths. (b) Normalized tensile strengths of the Kagome networks under the clamped boundary condition, in comparison with the effective tensile strengths under the periodic and roller boundary conditions.

clamped boundary condition, and Fig. 18(b) shows the effective strength of the Kagome networks. For $\varepsilon_f = 0.02$, the effective strength is similar to the damage initiation strength under the roller boundary condition, which is lower than that under the periodic boundary condition. For both the clamped and roller boundary conditions, the presence of the free edges lowers the effective tensile strength for the Kagome network with a relatively low fiber strength ($\varepsilon_f < 0.04$). In contrast, for a relatively high fiber strength ($\varepsilon_f \geq 0.04$), the effective tensile strength of the Kagome network under the clamped boundary condition is higher than that under the periodic or roller boundary condition. In this case, since buckling is largely suppressed by the clamped boundary condition, the effective stiffness of the Kagome network remains relatively high before damage initiation, and the effective tensile strength exceeds the critical stress for onset of buckling under the periodic boundary condition. For $\varepsilon_f = 0.1$, the effective tensile strength of the Kagome network under the clamped boundary condition is about twice of that under the periodic boundary condition. This result is independent of the network size as long as $n_x \gg n_y$.

Fig. 19(a) shows damage initiation and progression in a Kagome network of the relative density $\rho = 0.118$ with $\varepsilon_f = 0.1$, under the clamped boundary condition. The network remains elastic with stretch-dominated fiber deformation at the nominal strain $\varepsilon_y = 0.058$, with bending of fiber segments near the free edge. Damage initiation occurs at $\varepsilon_y = 0.06$, starting from the slanted fiber segments near the upper and lower corners of the free edge and almost instantaneously growing in the diagonal direction towards the mid-plane of the network. Subsequently, the damage grows like a crack along the mid-plane towards the center of the network. The strain energy is largely relaxed in the fibers behind the crack front, shown in blue. Ahead of the crack front, the strain energy density remains high in the fibers, shown in green and yellow. The highest strain energy density appears in a few fiber segments near the crack front, shown in red. The damage progression resembles steady-state crack growth in a long strip (Rivlin and Thomas, 1953). Notably, more than one layer of fiber segments are damaged along the crack.

Fig. 19(b) shows the vertical component of the reaction force along the upper edge of the Kagome network under the clamped boundary

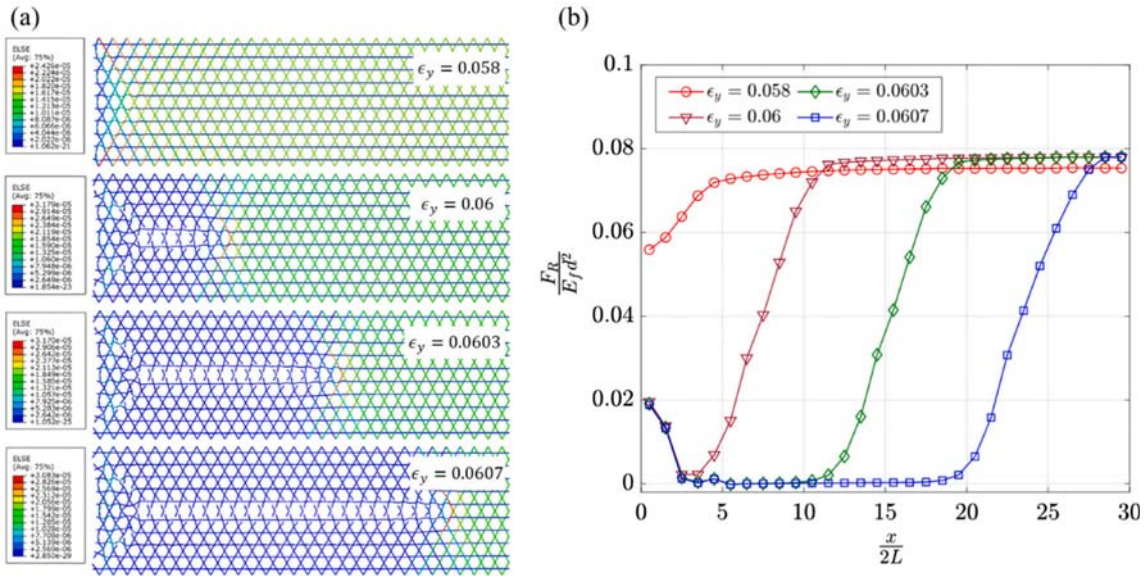

Fig. 19. (a) Damage initiation and progression in a Kagome network under the clamped boundary condition ($\rho = 0.118, \varepsilon_f = 0.1, n_x = 60, n_y = 5$), with color contours showing the strain energy density in the fibers. (b) Normalized reaction force (in the vertical direction) along the upper edge of the Kagome network, with increasing nominal strain ε_y.

condition. At $\varepsilon_y = 0.058$, the reaction force is slightly lower near the free edge and transitions to a constant in the center region. This is expected as the network is more compliant near the free edge. After damage initiation at $\varepsilon_y = 0.06$, the reaction force drops significantly near the free edge. Surprisingly, the reaction forces are not zero at the first two joints near the free edge, but drop to nearly zero at the next two joints. Further away from the free edge, the reaction force transitions to a constant value. As shown in Fig. 19(a), the crack-like defect appears to nucleate slightly away from the free edge, leaving behind a partially damaged boundary layer with some residual connectivity. By slightly increasing the nominal strain, the reaction force drops to nearly zero at increasingly more joints, with a steady-state transition to the undamaged part, while the partially damaged boundary layer near the free edge remains. The distribution of the reaction force clearly reflects the damage progression in the Kagome network shown in Fig. 19(a), with nucleation and growth of a crack-like defect.

6. Effect of crack-like defect

Consider finite-sized rectangular panels made from Kagome networks under the clamped boundary condition. Since damage initiation is likely to occur near the free edges, the presence of a crack-like defect at the free edges could influence the damage initiation and thus the effective strength of the Kagome network. Fig. 20(a) shows an example of a Kagome network with a crack-like defect at the free edge on the left side. The crack-like defect is introduced by removing two layers of slanted fiber segments between two horizontal fibers close to the middle plane of the network, similar to assuming that a layer of SS joints on the middle plane are damaged (Fleck and Qiu, 2007). In this section, we study the effect of the defect length (L_{crack}) on the effective strength, damage initiation and progression in the Kagome networks under the clamped boundary condition.

The inset of Fig. 20(b) shows that the stress–strain response of the Kagome network under the clamped boundary condition is linear before damage initiation, with an apparent stiffness decreasing with the normalized defect length. As shown in Fig. 20(a), the size of the network model is $n_x = 30$ and $n_y = 5$, with a symmetry boundary condition on the right side. The defect length (L_{crack}) is normalized by the length of the network model, $\bar{L}_{crack} = L_{crack}/L_x$, with $L_x = 2n_xL$ and L being the segment length. The apparent stiffness of the Kagome network with a crack-like defect is approximately linear with the defect length, namely

$$\bar{E}_{app} \approx \frac{3}{8}\rho E_f(1 - \bar{L}_{crack}) \tag{6.1}$$

Recall that $E_{eff} \approx \frac{1}{3}\rho E_f$ and $\bar{E}_{app} \approx \frac{9}{8}E_{eff}$ for the Kagome network with no defect. As shown in Fig. 20(b), the normalized stiffness ($\bar{E}_{app}/E_{eff}$) for two different relative densities, $\rho = 0.118$ and 0.02, are nearly identical, in good agreement with Eq. (6.1).

Assuming $\varepsilon_f = 0.1$ for the fiber material, Fig. 21 shows the effective stress–strain responses of the Kagome network ($\rho = 0.118$) with various defect lengths. When the defect size is small (e.g., $\bar{L}_{crack} = 0.0333$), the effective stress–strain response is similar to that with no defect ($\bar{L}_{crack} = 0$), but with a slightly lower effective strength. The effective stress of the network first drops to a lower level upon damage initiation at $\varepsilon_y \approx 0.0586$, and then increases slightly with the increasing nominal strain before dropping to nearly zero at $\varepsilon_y \approx 0.0624$. Such a stress–strain response suggests that damage progression is different due to the presence of a small defect, but damage initiation is similar to that with no defect. When the defect size is relatively large (e.g., $\bar{L}_{crack} = 0.167$), the effective strength is considerably lower, partly due to the reduced stiffness. In this case, damage initiation occurs at a smaller nominal strain ($\varepsilon_y \approx 0.0554$), but the effective stress drops slightly and then continues to increase until it reaches an ultimate strength at

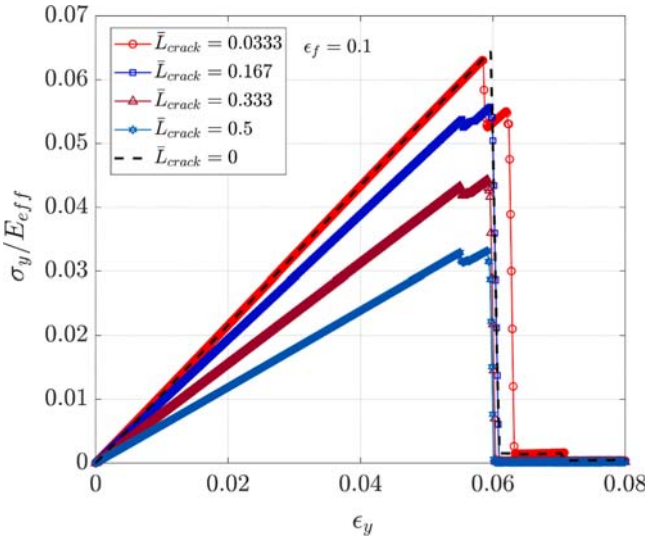

Fig. 21. Effective stress–strain curves for Kagome networks ($\rho = 0.118$ and $\varepsilon_f = 0.1$) with various defect lengths, subject to uniaxial tension with the clamped boundary condition.

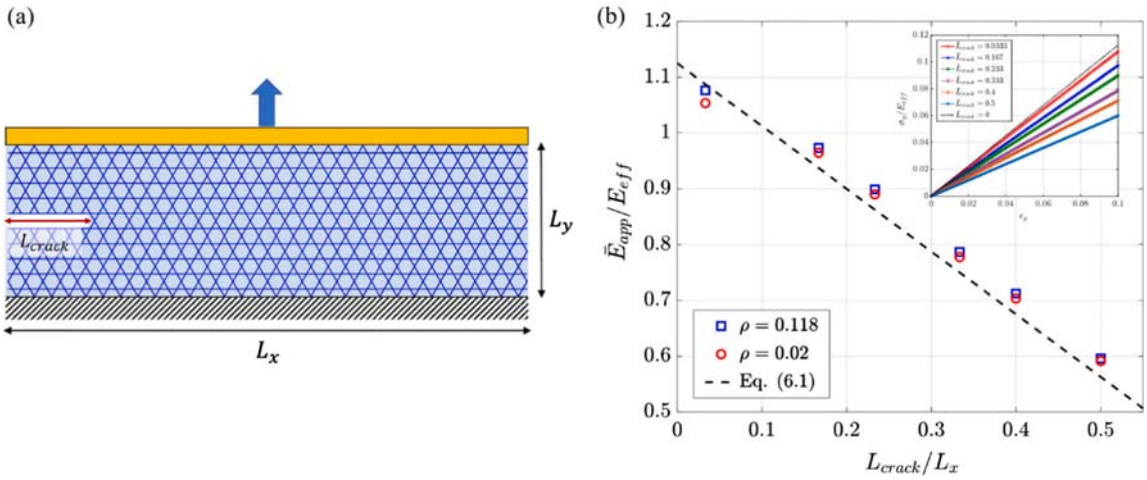

Fig. 20. (a) A Kagome network with a crack-like defect, subject to tension with the clamped boundary condition. (b) Apparent stiffness of the Kagome network as a function of the normalized defect length. Inset: Elastic stress–strain responses of the Kagome networks ($\rho = 0.118$), with a crack-like defect of various lengths.

$\varepsilon_y \approx 0.0596$. Such a stress–strain response suggests that, due to the presence of a relatively large defect, both the damage initiation and damage progression are different from the case with no defect. Notably, the nominal strains for the damage initiation and for the ultimate strength appear to be independent of the defect size as long as $\overline{L}_{crack} \geq 0.167$.

Fig. 22 shows the damage progression in the Kagome network with a small defect ($\overline{L}_{crack} = 0.0333$ or $L_{crack} = 2L$). At $\varepsilon_y = 0.0585$, just before damage initiation, the deformation is similar to that with no defect (Fig. 19a), with the highest strain energy density in the slanted fiber segments close to the upper/lower corners of the free edge (Fig. 22a). The presence of a small defect has little effect on the stress concentration at the corners. At $\varepsilon_y = 0.0587$, just after damage initiation, several fiber segments near the free edge are fractured, but not those near the small defect (Fig. 22b). The damage is distributed from the upper/lower corners to the mid-plane of the network, forming a crack-like feature slightly ahead of the small defect. At this point, the highest strain energy density appears in the slanted fiber segments at the front of the crack-like feature. Interestingly, this crack-like feature does not grow much until the nominal strain increases to $\varepsilon_y = 0.062$ (Fig. 22c), and then continues to grow in a steady state fashion (Fig. 22d). The steady-state damage progression corresponds to the sharp drop of the effective stress at $\varepsilon_y \approx 0.0624$ in Fig. 21. Compared to the Kagome network with no defect (Fig. 19), the damage initiation is similar, but the damage progression is different with the steady-state growth slightly delayed.

For a larger defect with $\overline{L}_{crack} = 0.167$ ($L_{crack} = 10L$), the strain energy density contour in Fig. 23(a) shows that the highest strain energy density before damage initiation ($\varepsilon_y = 0.0553$) occurs in the slanted fiber segments at the front of the crack-like defect, with no stress concentration at the corners. Consequently, damage initiates near the defect front at a lower nominal strain ($\varepsilon_y \approx 0.0554$) than that in Fig. 22. As the damage process continues with increasing nominal strain, the defect does not grow much until $\varepsilon_y = 0.06$, beyond which the damage progresses like steady-state crack growth. The corresponding reaction forces along the upper edge of the Kagome network are shown in Fig. 23

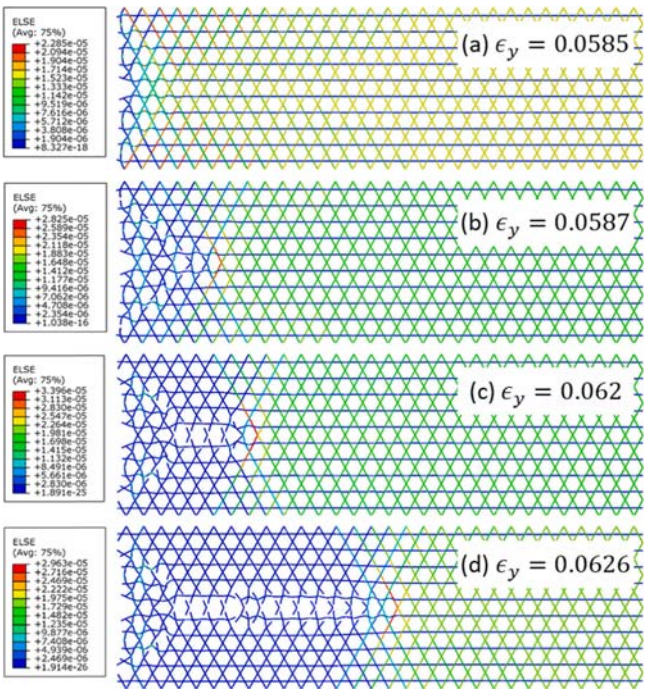

Fig. 22. Damage progression in a Kagome network with a small defect ($\rho = 0.118, \varepsilon_f = 0.1, \overline{L}_{crack} = 0.0333$). Color contours show the strain energy density in the fibers.

(b). Compared to the Kagome network with no defect (Fig. 19), both the damage initiation and progression are different, but the steady state is similar. Before damage initiation, the reaction forces near the free edge are much lower, due to the presence of the crack-like defect. During the steady-state growth, the reaction forces drop to nearly zero behind the crack front, with no residual connectivity near the free edge.

Fig. 24 shows that the location of damage initiation in the Kagome network with a crack-like defect depends on the length of the defect. As the defect length increases, the location of damage initiation shifts from the upper/lower corners of the free edge towards the front of the crack-like defect. A small defect (e.g., $\overline{L}_{crack} = 0.0333$ or $L_{crack} = 2L$) has little effect on damage initiation near the corners. In contrast, with a relatively long defect ($\overline{L}_{crack} > 0.1$ or $L_{crack} > 6L$), damage initiation occurs near the front of the defect at a lower nominal strain. Fig. 25(a) shows the critical nominal strain for damage initiation as a function of the length of the crack-like defect. With no defect ($L_{crack} = 0$), damage initiation occurs in the slanted fiber segments near the upper and lower corners of the free edge. The critical strain for damage initiation is approximately proportional to the fiber strength, with $\varepsilon_{yc}/\varepsilon_f \approx 0.6$ for $\varepsilon_f = 0.1$ and 0.06. With a small defect ($\overline{L}_{crack} < 0.1$), the critical strain for damage initiation remains similar. However, with a relatively long defect ($\overline{L}_{crack} > 0.1$), the critical strain for damage initiation is lower, $\varepsilon_{yc}/\varepsilon_f \approx 0.55$, and is nearly independent of the defect length. As the defect length increases, the change in the critical strain for damage initiation correlates with the location of damage initiation in Fig. 24. Once the defect length is greater than a fraction of L_y, damage initiation occurs at the front of the defect, and the critical strain becomes independent of the defect length.

Fig. 25(b) shows the effective strength corresponding to damage initiation in the Kagome networks ($\rho = 0.118$) with a crack-like defect. With no defect ($L_{crack} = 0$), the effective strength normalized by the fiber strength is approximately $S_{eff}/S_f \approx 0.0256$ for $\varepsilon_f = 0.1$ and 0.06, according to Fig. 18(b). With a small defect ($\overline{L}_{crack} < 0.1$), the effective strength is nearly independent of the defect size and thus flaw tolerant as noted by Fleck and Qiu (2007). In contrast, with a relatively long defect ($\overline{L}_{crack} > 0.1$), the effective strength decreases almost linearly with the length of the crack-like defect. With a constant critical strain, $\varepsilon_{yc}/\varepsilon_f \approx 0.55$ for $\rho = 0.118$ (Fig. 25a), and an apparent stiffness under the clamped boundary condition by Eq. (6.1), $\overline{E}_{app} \approx \frac{3}{8}\rho E_f(1 - \overline{L}_{crack})$, the effective tensile strength is obtained approximately as:

$$S_{eff} = \overline{E}_{app}\varepsilon_{yc} \approx 0.0243(1 - \overline{L}_{crack})S_f \tag{6.2}$$

As shown in Fig. 25(b), the numerical results are in good agreement with Eq. (6.2) for the cases with a relatively long defect ($\overline{L}_{crack} > 0.1$), where the effective strength decreases primarily due to the reduced stiffness $\overline{E}_{app}$. We note that the critical strain for damage initiation, $\varepsilon_{yc}/\varepsilon_f$, may depend on the relative density of the network, so that the normalized effective strength, S_{eff}/S_f, would depend on the relatively density accordingly.

6.1. Discussion on damage initiation

The critical strain for damage initiation in a Kagome network may be used to estimate its effective fracture toughness. Fleck and Qiu (2007) calculated the effective fracture toughness of a Kagome network by assuming that the individual fiber segments behave as elastic-brittle beams and fail when the maximum local tensile stress at any point attains the strength of the fiber material, (S_f). They found that the mode-I fracture toughness (in terms of the critical stress intensity factor) of the Kagome network scales with the relative density according to

$$K_{Ic} = DS_f\sqrt{\rho L}, \tag{6.3}$$

where $D = 0.212$. Corresponding to the critical stress intensity factor,

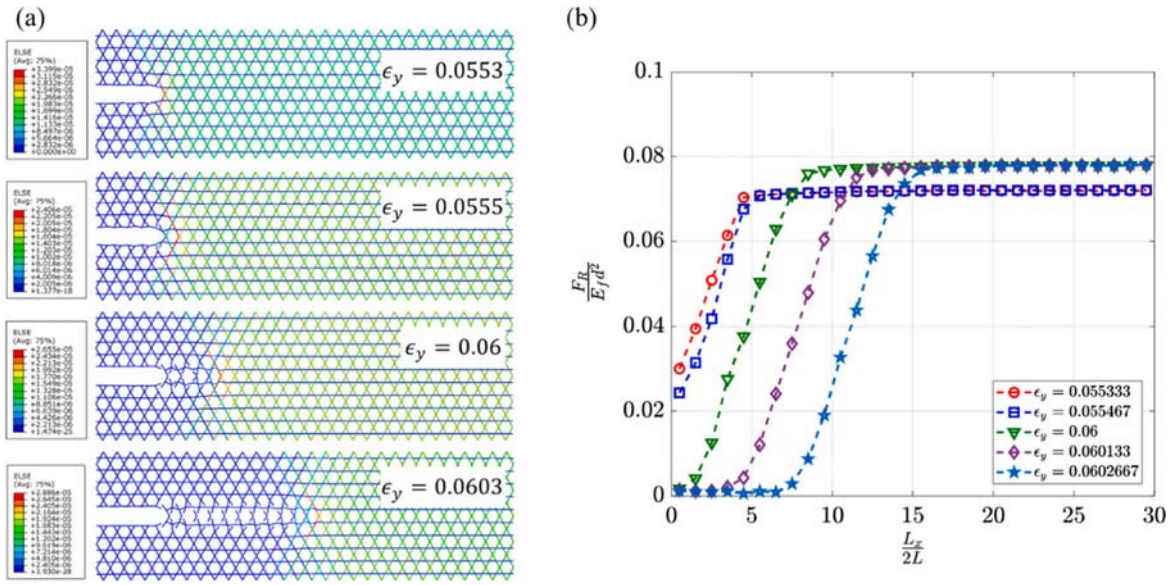

Fig. 23. Damage progression in a Kagome network with a crack-like defect ($\rho = 0.118, \varepsilon_f = 0.1, \bar{L}_{crack} = 0.167$). (a) Color contours show the strain energy density in the fibers at increasing nominal strain ε_y; (b) Normalized reaction force (in the vertical direction) along the upper edge of the Kagome network, with increasing nominal strain ε_y.

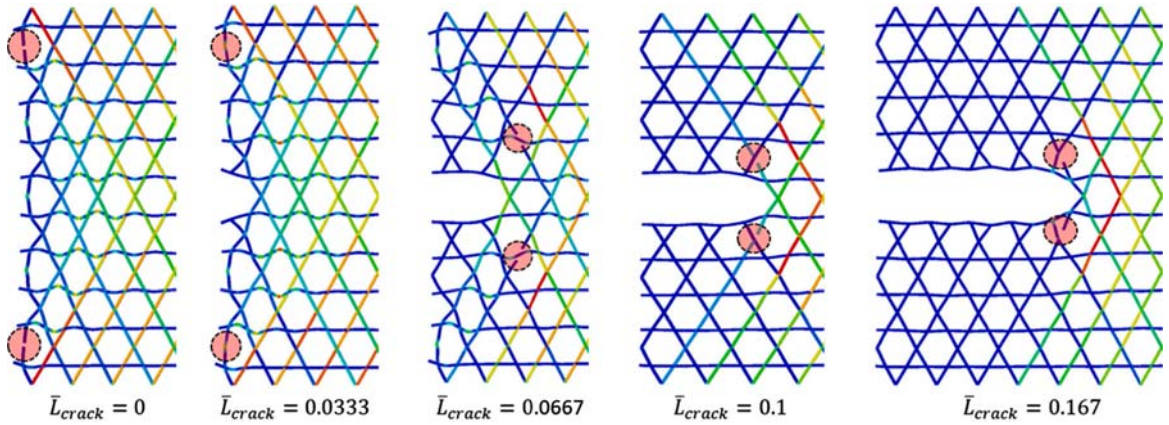

Fig. 24. Locations of damage initiation in the Kagome networks ($\rho = 0.118$ and $\varepsilon_f = 0.1$) with a crack-like defect of various lengths.

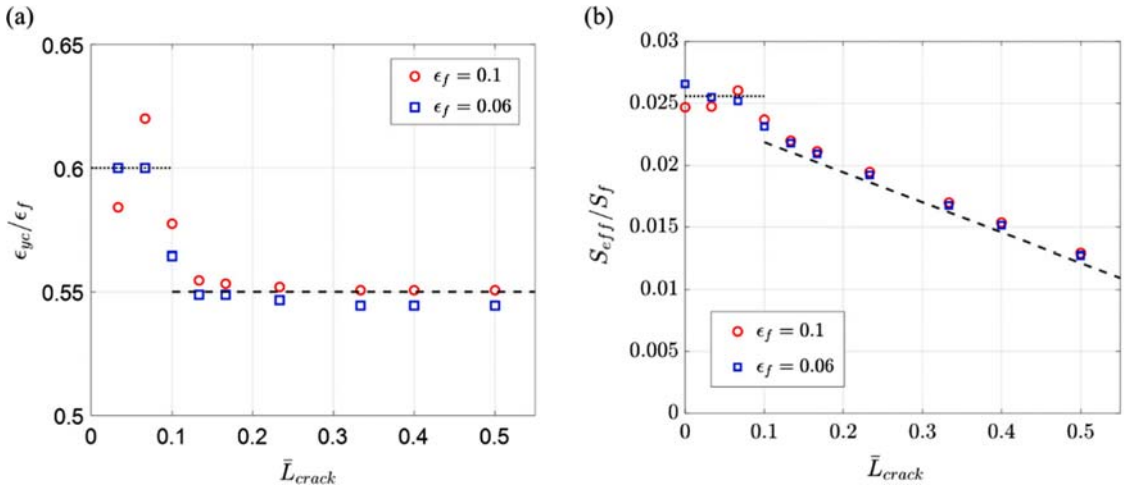

Fig. 25. (a) Critical nominal strain for damage initiation in Kagome networks ($\rho = 0.118$) with a crack-like defect of various lengths and two fiber strengths. (b) Effective strength for damage initiation, normalized by the fiber strength. The dashed line is predicted by eq. (6.2).

the effective toughness of the Kagome network in terms of energy release rate is:

$$\Gamma_{eff} = \frac{K_{Ic}^2}{E_{eff}} = 3D^2 E_f \varepsilon_f^2 L. \tag{6.4}$$

Remarkably, this predicted Γ_{eff} is independent of the relative density for Kagome networks.

For a Kagome network with a relatively long crack-like defect (Fig. 20a), subject to tension with the clamped boundary condition, damage initiation occurs near the crack front. In this case, the energy release rate can be estimated as in a pure shear test (Rivlin and Thomas, 1953), namely

$$G = \frac{1}{2}\frac{E_{eff}}{1-\nu_{eff}^2}\varepsilon_y^2 L_y. \tag{6.5}$$

By setting $G = \Gamma_{eff}$ in Eq. (6.4), we obtain the critical strain for damage initiation as

$$\varepsilon_{yc} = 4D\varepsilon_f \sqrt{\frac{L}{\rho L_y}}. \tag{6.6}$$

For $\rho = 0.118$ and $n_y = 5$ ($L_y/L = 10\sqrt{3}$), Eq. (6.6) predicts that $\varepsilon_{yc}/\varepsilon_f = 0.593$, which is slightly higher than the numerical results, $\varepsilon_{yc}/\varepsilon_f \approx 0.55$, for relatively long crack-like defects ($\bar{L}_{crack} > 0.1$) shown in Fig. 25(a). By Eq. (6.6), the critical strain for damage initiation depends on the relative density ρ and the network size L_y/L. However, this dependence has not been confirmed numerically.

It is noted that by Eq. (6.6) we have assumed that the critical energy release rate for a Kagome network with the clamped boundary condition in the present study is the same as that determined by Fleck and Qiu (2007) using the K-field approach. Both are symmetric mode-I fracture. In other words, Eq. (6.4) is taken as the effective material property of the Kagome network, so that the criterion for fracture initiation is: $G = \Gamma_{eff}$. The underlying assumption is that the damage processes are the same for the same Kagome networks, even though the elastic K-field may not exist in the present model with 5 layers of unit cells (Fig. 20a). As can be seen in Fig. 23, the damage processes are confined within a couple layers of unit cells near the crack-like defect, and thus the present model is large enough to contain the damage process zone. The energy approach does not require the presence of an elastic K-field. As long as the damage process zone is fully contained in the present model, the same critical energy release rate is expected as the effective material property.

6.2. Discussion on steady-state damage progression

Next we discuss the steady-state damage progression. It is noted from Fig. 23 that the steady-state damage progression occurs at a higher strain, $\varepsilon_{SS} \approx 0.6\varepsilon_f$, for the Kagome networks with $\rho = 0.118$ and $n_y = 5$ ($L_y/L = 10\sqrt{3}$). By setting $\varepsilon_y = \varepsilon_{SS}$ in Eq. (6.5), the energy release rate for the steady-state crack growth is obtained as:

$$G_{SS} = 0.138 E_f {\varepsilon_f}^2 L \tag{6.7}$$

which is slightly higher than the effective toughness Γ_{eff} in Eq. (6.4). If we assume that, like Γ_{eff} in Eq. (6.4), G_{SS} is a constant independent of the network size (n_y) or the relative density (ρ), G_{SS} in Eq. (6.7) can be treated as an effective material property of Kagome networks, so that the strain for steady-state damage progression can be predicted for other Kagome networks as

$$\varepsilon_{SS} = \sqrt{\frac{2G_{SS}}{\bar{E}_{eff} L_y}} = 0.46\varepsilon_f (\rho n_y)^{-1/2}. \tag{6.8}$$

The steady-state strain predicted by Eq. (6.8) depends on the network size n_y and the relative density ρ. The predicted dependence on the network size agrees reasonably well with the numerical results shown in Fig. 26 for $\rho = 0.118$ and two different values of ε_f. However, the predicted dependence on the relative density has not been confirmed numerically.

The assumption that the steady-state energy release rate G_{SS} is independent of the relative density (ρ) may be questionable. Here, we propose an alternative approach to estimating the steady-state energy release rate by following the Lake-Thomas model for polymer networks (Lake and Thomas, 1967). Assume that a crack grows in the steady state by cutting through one layer of unit cells, so that four slanted fiber segments per unit cell are fractured and the elastic strain energy in the four fiber segments is dissipated by brittle fracture. Let $U_f = \frac{1}{2}E_f\varepsilon_f^2$ be the maximum strain energy density in each fiber segment under tension, which is dissipated upon fracture, and we obtain the steady-state fracture toughness by the energy dissipation per unit area of crack growth as:

$$\Gamma_{SS} = \frac{4U_f V_f}{A_{uc}} = \frac{1}{\sqrt{3}}\rho E_f \varepsilon_f^2 L, \tag{6.9}$$

where $V_f = d^2 L$ (volume of each fiber segment) and $A_{uc} = 2Ld$ (cross sectional area of each unit cell). When the crack grows in the steady state, the energy release rate equals the fracture toughness, $G_{SS} = \Gamma_{SS}$. It is found that Eq. (6.9) underestimates the steady-state energy release rate in Eq. (6.7) by a factor of ~ 2 (for $\rho = 0.118$). This discrepancy can be attributed to the fact that more than four fiber segments are fractured as the crack grows by each unit cell, as shown in Fig. 23(a). Therefore, Eq. (6.9) predicts the lower bound for the steady-state toughness of the Kagome network, similar to the Lake-Thomas model for polymer networks (Lake and Thomas, 1967; Yang et al., 2019; Deng et al., 2023). Following a similar approach, Luan et al. (2022) estimated the critical energy release rate (by fracturing a single strut) for triangular and hexagonal lattices, and they obtained similar scaling as in Eq. (6.9). However, in comparison with experiments, they found that the approximate critical energy release rates underestimated the critical stresses for both triangular and hexagonal lattices. In the case of the Kagome networks in the present study, the predicted toughness would double if eight (instead of four) fiber segments are fractured as the crack grows by each unit cell, including those segments above/below the crack plane. Thus, the fracture toughness of the network can be increased by the distributed damage around the crack, similar to polymer networks with imperfections (Yang et al., 2019) or non-local energy dissipation (Deng et al., 2023).

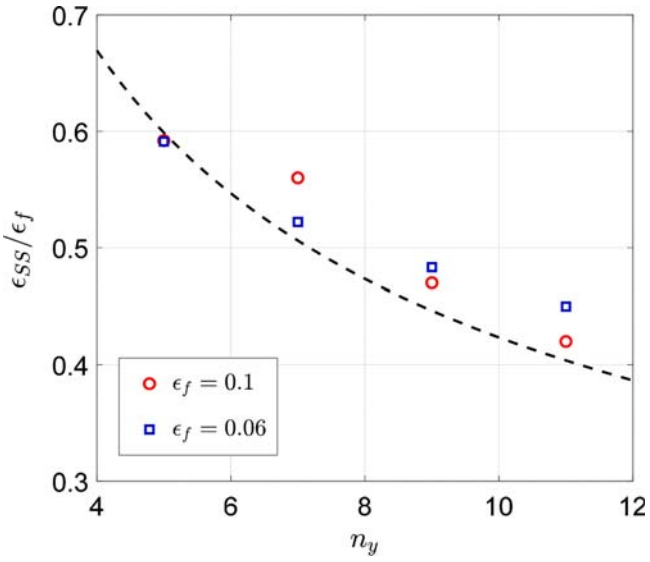

Fig. 26. Strain for steady-state damage progression in Kagome networks ($\rho = 0.118$) of various network sizes (n_y).

Remarkably, Eq. (6.9) predicts that the steady-state energy release rate scales linearly with the relative density ρ, in contrast with the effective toughness Γ_{eff} in Eq. (6.4) for damage initiation, which is independent of the relative density. On the other hand, Fleck and Qiu (2007) found that $K_{Ic} \sim \rho$ for triangular lattices and $K_{Ic} \sim \rho^2$ for the hexagonal lattices, both of which would lead to a linear scaling for the effective toughness, $\Gamma_{eff} = \frac{K_{Ic}^2}{E_{eff}} \sim \rho$. Similarly scaled critical energy release rates were also obtained by Luan et al. (2022) for triangular and hexagonal lattices by an energy-based approach. However, for the Kagome lattices, $K_{Ic} \sim \rho^{1/2}$ according to Fleck and Qiu (2007), so that $\Gamma_{eff} \sim \rho^0$ (independent of ρ), differing from both triangular and hexagonal lattices. It would be interesting to investigate further if and how the effective toughness Γ_{eff} and the steady-state energy release rate G_{SS} of the Kagome network depend on the relative density. If G_{SS} is independent of the relative density, similar to Γ_{eff} by Eq. (6.4), the corresponding strain for the steady state would depend on the relative density, $\varepsilon_{SS} \sim \rho^{-1/2}$, as predicted by Eq. (6.8). In contrast, if G_{SS} depends on the relative density ($G_{SS} \sim \rho$) following Eq. (6.9), the critical strain for the steady state damage progression can be obtained from Eq. (6.5) as:

$$\varepsilon_{SS} = \sqrt{\frac{2G_{SS}}{\bar{E}_{eff} L_y}} = \frac{4}{3}\varepsilon_f (2n_y)^{-1/2}, \tag{6.10}$$

which is independent of the relative density, but with the same dependence on the network size n_y as in Eq. (6.8). At the moment, we do not have any data or evidence to say either Eq. (6.8) or Eq. (6.10) is valid or invalid. The dependence of the steady-state strain on the relative density can be used to determine the dependence of the steady-state toughness on the relative density. We leave it as an open question for future studies to determine the steady-state toughness of Kagome networks, for which the pure-shear configuration (Fig. 20a) with a relatively long crack-like defect can be used as a simple but robust setup for both experiments and simulations.

7. Summary

We have conducted a numerical study on the tensile strength of low-density Kagome networks made of linearly elastic and brittle fibers. The main findings are summarized as follows.

- First, an elastic beam model is employed to analytically predict the effective elastic properties and tensile strength, as well as the critical condition for buckling of the fibers in Kagome networks. In particular, while the linear elastic properties of a Kagome network are isotropic, the tensile strength is anisotropic, and can be reduced by buckling.
- A finite element method is developed to simulate the elastic deformation and failure of Kagome networks under tension. The numerical results from unit-cell models reveal four possible damage-initiation failure modes of the Kagome networks subject to uniaxial tension, including both pre-buckling and post-buckling failure modes, summarized in a phase diagram in terms of the relative density and the fiber strength. In particular, a low-density Kagome network is likely to fail by one of the post-buckling modes, with an effective tensile strength much lower than the prediction of the elastic beam model.
- For Kagome networks consisting of a large number of unit cells, the effect of boundary conditions on the tensile strength is examined (Fig. 18b). Under periodic boundary conditions, the effective tensile strength is nearly identical to that predicted by the unit-cell model. Under a roller boundary condition, the effective tensile strength is lower than that under periodic boundary conditions for low fiber strength, but is similar for relatively high fiber strength. Under a clamped boundary condition, the effective tensile strength is similar to that under the roller boundary condition for low fiber strength, but is higher for relatively high fiber strength.
- Finally, the effect of a crack-like defect on the effective tensile strength is studied for Kagome networks under the clamped boundary condition. With a small defect, the effective strength is nearly independent of the defect size. In contrast, with a relatively long defect, the effective strength decreases almost linearly with the length of the crack-like defect. The effective toughness for damage initiation and steady-state damage progression in the Kagome networks are estimated and discussed from an energetic perspective. It is suggested that the steady-state toughness of Kagome networks can be determined by using the pure-shear configuration (Fig. 20a) with a relatively long crack-like defect as a simple but robust setup for both experiments and simulations.

CRediT authorship contribution statement

Soham M. Mane: Writing – review & editing, Writing – original draft, Visualization, Software, Methodology, Investigation, Formal analysis. **Kenneth M. Liechti:** Writing – review & editing, Methodology, Investigation, Funding acquisition, Conceptualization. **Rui Huang:** Writing – review & editing, Supervision, Project administration, Methodology, Investigation, Funding acquisition, Conceptualization.

Declaration of competing interest

The authors declare that they have no known competing financial interests or personal relationships that could have appeared to influence the work reported in this paper.

Data availability

Data will be made available on request.

Acknowledgements

We gratefully acknowledge partial funding of this work by the Center for Dynamics and Control of Materials (CDCM) supported by the National Science Foundation (NSF) under Award No. DMR1720595.

References

Boyce, M.C., Arruda, E.M., 2000. Constitutive models of rubber elasticity: a review. Rubber Chem. Technol. 73, 504–523.
Christensen, R.M., 2000. Mechanics of cellular and other low-density materials. Int. J. Solids Struct. 37, 93–104.
Cui, X., Xue, Z., Pei, Y., Fang, D., 2011. Preliminary study on ductile fracture of imperfect lattice material. Int. J. Solids Struct. 48, 3453–3461.
Deng, B., Wang, S., Hartquist, C., Zhao, X., 2023. Nonlocal Intrinsic Fracture Energy of Polymerlike Networks. Phys. Rev. Lett. 131, 228102.
Fleck, N.A., Deshpande, V.S., Ashby, M.F., 2010. Micro-architectured materials: past, present and future. Proc. R. Soc. A 466, 2495–2516.
Fleck, N.A., Qiu, X., 2007. The damage tolerance of elastic-brittle, two-dimensional isotropic lattices. J. Mech. Phys. Solids 55, 562–588.
Gibson, L., Ashby, M., 1997. Cellular Solids-Structure and Properties. Cambridge University Press.
Gu, H., Pavier, M., Shterenlikht, A., 2018. Experimental study of modulus, strength and toughness of 2D triangular lattices. Int. J. Solids Struct. 152–153, 207–216.
Lake, G.J., Thomas, A.G., 1967. The strength of highly elastic materials. Proc. R. Soc. Lond. Series A. Math. Phys. Sci. 300, 108–119.
Lipperman, F., Ryvkin, M., Fuchs, M.B., 2007. Fracture toughness of two-dimensional cellular material with periodic microstructure. Int. J. Fract. 146, 279–290.
Liu, Y., St-Pierre, L., Fleck, N.A., Deshpande, V.S., Srivastava, A., 2020. High fracture toughness micro-architectured materials. J. Mech. Phys. Solids 143, 104060.
Lu, Q., Gao, W., Huang, R., 2011. Atomistic simulation and continuum modeling of graphene nanoribbons under uniaxial tension. Model. Simul. Mater. Sci. Eng. 19, 054006.
Luan, S., Chen, E., Gaitanaros, S., 2022. Energy-based fracture mechanics of brittle lattice materials. J, Mech. Phys. Solids 169, 105093.
Mane, S.M., 2023. A Numerical Study on Mechanical Properties of Low-Density Two-Dimensional Networks of Crosslinked Long Fibers. University of Texas at Austin. PhD dissertation.

Mane, S.M., Khabaz, F., Bonnecaze, R.T., Liechti, K.M., Huang, R., 2021. A numerical study on elastic properties of low-density two-dimensional networks of crosslinked long fibers. Int. J. Solids Struct. 230–231, 111164.
Meza, L.R., Das, S., Greer, J.R., 2014. Strong, lightweight, and recoverable three-dimensional ceramic nanolattices. Science 345 (6202), 1322–1326.
Meza, L.R., Zelhofer, A.J., Clarke, N., Mateos, A.J., Kochmann, D.M., Greer, J.R., 2015. Resilient 3D hierarchical architected metamaterials. PNAS 112 (37), 11502–11507.
Needleman, A., Tvergaard, V., 1992. Analyses of plastic flow localization in metals. Appl. Mech. Rev. 45 (3S), S3–S18. https://doi.org/10.1115/1.3121390.
Ostoja-Starzewski, M., 2002. Lattice models in micromechanics. Appl. Mech. Rev., 55 (1) (2002), pp. 35-60.
Quintana Alonso, I., Fleck, N.A., 2009. Compressive response of a sandwich plate containing a cracked diamond-celled lattice. J. Mech. Phys. Solids 57, 1545–1567.
Quintana Alonso, I., Mai, S.P., Fleck, N.A., Oakes, D.C.H., Twigg, M.V., 2010. The fracture toughness of a cordierite square lattice. Acta Mater. 58, 201–207.
Rivlin, R.S., Thomas, A.G., 1953. Rupture of rubber. I. Characteristic energy for tearing. J. Poly. Sci. 3, 291–318.
Romijn, N.E.R., Fleck, N.A., 2007. The fracture toughness of planar lattices: Imperfection sensitivity. J. Mech. Phys. Solids 55 (12), 2538–2564.
Schwaiger, R., Meza, L.R., Li, X., 2019. The extreme mechanics of micro- and nanoarchitected materials. MRS Bull. 44, 758–765.
Shaikeea, A.J.D., Cui, H., O'Masta, M., Zheng, X.R., Deshpande, V.S., 2022. The toughness of mechanical metamaterials. Nat. Mater. 21, 297–304.
Tankasala, H.C., Deshpande, V.S., Fleck, N.A., 2015. Crack-tip fields and toughness of two-dimensional elasto-plastic lattices. J. Appl. Mech. 82, 091004.
Wang, A.-J., McDowell, D.L., 2004. In-plane stiffness and yield strength of periodic metal honeycombs. J. Eng. Mater. Technol. 126 (2), 137–156.
Xia, X., Afshar, A., Yang, H., Portela, C.M., Kochmann, D.M., Di Leo, C.V., Greer, J.R., 2019. Electrochemically reconfigurable architected materials. Nature 573, 205–213.
Yang, C., Yin, T., Suo, Z., 2019. Polyacrylamide hydrogels. I. Network Imperfection. J. Mech. Phys. Solids 131, 43–55.
Zhang, X., Vyatskikh, A., Gao, H., Greer, J.R., Li, X., 2019. Lightweight, flaw-tolerant, and ultrastrong nanoarchitected carbon. Proc. Natl. Acad. Sci., 116 (14) (2019), pp. 6665-6672.